

**THE RAPID INTENSIFICATION OF HURRICANE KARL (2010): NEW  
REMOTE SENSING OBSERVATIONS OF CONVECTIVE BURSTS  
FROM THE GLOBAL HAWK PLATFORM**

Stephen R. Guimond<sup>1,2</sup>, Gerald M. Heymsfield<sup>2</sup>, Paul D. Reasor<sup>3</sup>, and Anthony C.  
Didlake, Jr.<sup>2,4</sup>

<sup>1</sup>*University of Maryland/Earth System Science Interdisciplinary Center (ESSIC), College  
Park, Maryland*

<sup>2</sup>*NASA Goddard Space Flight Center, Greenbelt, Maryland*

<sup>3</sup>*NOAA Hurricane Research Division, Miami, Florida*

<sup>4</sup>*Oak Ridge Associated Universities, Oak Ridge, Tennessee*

Submitted to the *Journal of the Atmospheric Sciences*

January 14, 2016

*Corresponding author address:* Stephen R. Guimond, NASA Goddard Space Flight  
Center, Code 612, Greenbelt, MD 20771.  
E-mail: [stephen.guimond@nasa.gov](mailto:stephen.guimond@nasa.gov)

## ABSTRACT

The evolution of rapidly intensifying Hurricane Karl (2010) is examined from a suite of remote sensing observations during the NASA Genesis and Rapid Intensification Processes (GRIP) field experiment. The novelties of this study are in the analysis of data from the airborne Doppler radar HIWRAP and the new Global Hawk airborne platform that allows long endurance sampling of hurricanes. Supporting data from the HAMSr microwave sounder coincident with HIWRAP and coordinated flights with the NOAA WP-3D aircraft help to provide a comprehensive understanding of the storm. The focus of the analysis is on documenting and understanding the structure, evolution and role of small scale, deep convective forcing in the storm intensification process.

Deep convective bursts are sporadically initiated in the downshear quadrants of the storm and rotate into the upshear quadrants for a period of  $\sim 12$  h during the rapid intensification. The aircraft data analysis indicates that the bursts are forming through a combination of two main processes: (1) convergence generated from counter-rotating mesovortex circulations and the larger scale flow and (2) the turbulent transport of warm, buoyant air from the eye to the eyewall at mid-to-low levels. The turbulent mixing across the eyewall interface and forced convective descent adjacent to the bursts assists in carving out the eye of Karl, which leads to an asymmetric enhancement of the warm core. The mesovortices play a key role in the evolution of the features described above.

The Global Hawk aircraft allowed an examination of the vortex response and axisymmetrization period in addition to the burst pulsing phase. A pronounced axisymmetric development of the vortex is observed following the pulsing phase that includes a sloped eyewall structure and formation of a clear, wide eye.

## 1. Introduction

The intensification of tropical cyclones (TCs) is a complex process that is governed by nonlinear coupling of physics across a vast array of space and time scales. On the slow/large scales, a sufficiently warm ocean and low vertical wind shear have been identified as providing favorable environmental conditions for the intensification of TCs (e.g. Kaplan and DeMaria 2003). On the fast/small scales, a large body of evidence has shown that deep, rotating, convective towers are responsible for the intensification, including rapid intensification (RI), of TCs (Steranka et al. 1986; Simpson et al. 1998; Heymsfield et al. 2001; Kelley et al. 2004; Montgomery et al. 2006; Braun et al. 2006; Reasor et al. 2009; Guimond et al. 2010; Molinari and Vollaro 2010; Rogers et al. 2015).

It is the fast/small scales that are the most challenging for the observation, numerical modeling and understanding of TCs. Deep convective towers in TCs have lifetimes of an hour or less with horizontal scales less than 10 km (Montgomery et al. 2006; Houze et al. 2009; Guimond et al. 2010) making it difficult to observe their kinematic properties, especially from conventional aircraft, which can only sample storms for short periods of time ( $\sim 5$  h). The turbulent, highly nonlinear character of deep convective towers and their interaction with the TC vortex are major challenges for numerical models and our physical understanding because those scales not explicitly resolved must be parameterized, which are not always adequate (e.g. Persing et al. 2013) and there can be considerable sensitivity to the algorithms used to solve the fluid-flow equations (e.g. Guimond et al. 2016).

The dynamics responsible for the rapid intensification of TCs from localized, deep convection project onto two classes of modes relative to the storm center: axisymmetric

95 and asymmetric. In the axisymmetric framework, the projection of localized heat forcing  
96 onto the azimuthal mean results in rings of heating typically maximized inside the radius  
97 of maximum winds for intensifying storms. Rogers et al. (2013) analyzed a large set of  
98 airborne Doppler radar composites of intensifying and steady-state TCs and discovered  
99 that a key characteristic of intensifying TCs is the location of deep convective towers  
100 inside the radius of maximum winds (RMW). Earlier studies by Schubert and Hack  
101 (1982) and Nolan et al. (2007) have elucidated the dynamics of intensifying hurricane  
102 vortices finding that convective heating placed inside the RMW enables more efficient  
103 conversion of potential to kinetic energy due to the increased inertial stability of the  
104 vortex.

105       The heating rings drive an axisymmetric secondary circulation with radial inflow at  
106 low levels, updrafts through the core of the heating and radial outflow aloft. In the  
107 azimuthal mean, the vortex intensifies through the radial convergence of absolute angular  
108 momentum, which is materially conserved above the boundary layer. This framework  
109 has been understood for many years (e.g. Shapiro and Willoughby 1982). Other  
110 axisymmetric theories for TC intensification have been presented such as the work of  
111 Emanuel (1986) and Rotunno and Emanuel (1987), which focus on the cycling of energy  
112 extracted through the thermodynamic disequilibrium at the air-ocean interface.

113       In the asymmetric framework, the heating and vorticity asymmetries generated from  
114 localized convective forcing interact with the mean flow through eddy heat and  
115 momentum fluxes, which can lead to intensification of the vortex for up-gradient  
116 transport (Montgomery and Kallenbach 1997). This process is generally called  
117 “axisymmetrization” and has been shown to occur in observational (e.g. Reasor et al.

2000;Reasor et al. 2009) and modeling (e.g. Montgomery et al. 2006;Persing et al. 2013) studies. In nature, the axisymmetric and asymmetric modes are coupled to one another with axisymmetric processes often playing the largest role (e.g. Nolan and Grasso 2003), but with asymmetric dynamics contributing a significant, non-negligible component of the overall system intensification (e.g. Montgomery et al. 2006; Persing et al. 2013; Guimond et al. 2016).

In addition to these effects, deep convective towers have also been observed to initiate localized interaction between the eye and eyewall. For example, the studies of Heymsfield et al. (2001) and Guimond et al. (2010), which analyzed very high resolution airborne radar data (along-track sampling of 100 m), showed that deep convective towers intensified the warm core through compensating subsidence around strong updrafts and its turbulent transport towards the eye. This intense, localized transport of air from the eyewall to the eye has important implications for storm intensification through the attendant inward flux of angular momentum.

The purpose of this paper is to analyze the rapid intensification (RI) of Hurricane Karl (2010), which coincided with a convective burst episode, from a suite of remote sensing observations to understand more details of the dynamics occurring on the fast/small scales. The novelties of this study are in the use of a new airborne radar and a new airborne platform for hurricane research that allows long endurance (up to 24 h) sampling. Details of these new technologies will be discussed in the next section.

## **2. Data and processing**

### *a. HIWRAP*

The High-Altitude Imaging Wind and Rain Airborne Profiler (HIWRAP) is an airborne Doppler radar that was developed at the NASA Goddard Space Flight Center (GSFC) with the goal of studying hurricanes and other precipitating systems. One of the unique features of HIWRAP is its ability to fly on NASA's Global Hawk (GH) unmanned aircraft, which operates at  $\sim 18 - 19$  km ( $60 - 62$  kft) altitude and can remain airborne for  $\sim 24$  h. The long endurance of the GH is a significant capability for hurricane research. Hurricanes form over remote regions of the ocean with important physical processes occurring on fast time scales that can be easily missed by conventional aircraft that can only remain airborne for  $\sim 6$  h.

HIWRAP is a dual-frequency (Ku- and Ka- band), single-polarized (V for inner beam, H for outer beam), downward pointing and conically scanning (16 rpm) Doppler radar with two beams ( $\sim 30^\circ$  and  $40^\circ$  tilt angles) and 150 m range resolution. The GH aircraft has an airspeed of  $\sim 160$  m s<sup>-1</sup>, which yields  $\sim 600$  m along-track sampling for HIWRAP. More details on HIWRAP can be found in Li et al. (2015).

The NASA Genesis and Rapid Intensification Processes (GRIP) experiment in 2010 was the first time HIWRAP collected significant data and some issues with the data quality (e.g. excessive noise at Ku-band due to a variety of issues including pulse processing) were found. To address these issues, we have done two things: (1) pulse pair estimates at Ku-band were reprocessed with 128 pulses averaged (azimuthal resolution of  $\sim 2.8^\circ$ ), which improves the signal-to-noise ratio (SNR) over the original averaging interval of 64 pulses and (2) Ku-band wind retrievals below the noise saturation level (determined using a power threshold, which translates to  $\sim 25$  dBZ at 3 km height) were replaced with the corresponding Ka-band wind retrievals, which provide a higher SNR

and thus, lower uncertainty Doppler velocities in these regions. In the flights over Karl presented in this work, only the inner ( $30^\circ$ ) beam was functional, which provides a swath width at the surface of  $\sim 20 - 22$  km.

Retrievals of the three-dimensional wind vector over the entire radar sampling volume are performed with the three-dimensional variational (3DVAR) algorithm described in Guimond et al. (2014). The 3DVAR method combines an observational error term as well as constraints that include the anelastic mass continuity equation, a Laplacian filter and the impermeability condition at the surface. A coefficient of  $2\Delta x^2$  was used for the mass continuity constraint and  $0.5\Delta x^4$  was used for the filtering constraint with  $\Delta x$  representing the horizontal grid spacing. These values were chosen based on wind vector solution sensitivity tests that provided reasonable accuracy and damping characteristics. The retrievals are performed on a storm-following grid with a horizontal grid spacing of 1 km and vertical spacing of 1 km. Retrievals with vertical spacing of  $\sim 150$  m are possible, but 1 km spacing was deemed sufficient for the present study. NOAA's Hurricane Research Division (HRD), using the Willoughby and Chelmow (1982) method, provided storm center estimates. The mean storm motion vector averaged over the aircraft-sampling period was removed from the HIWRAP derived horizontal winds.

Guimond et al. (2014) showed that simulated and *in situ* errors for the horizontal wind components were  $\sim 2.0 \text{ m s}^{-1}$  or  $\sim 7 \%$  of the hurricane wind speed. The errors in the vertical velocity were strongly dependent on the across-track location of the measurements with comparisons to *in situ* data revealing errors of  $\sim 2.0 \text{ m/s}$  at nadir. These *in situ* errors used data from the Imaging Wind and Rain Airborne Profiler

(IWRAP) flying on the NOAA P3 aircraft, which has a similar scanning geometry to HIWRAP. The appendix presents comparisons of *in situ* data to HIWRAP retrievals, which reveal that for wind speeds  $> 10 \text{ m s}^{-1}$  the mean error in the computed wind speed and direction is  $\sim 1 - 4 \text{ m s}^{-1}$  and  $\sim 10 - 20^\circ$ , respectively.

#### *b. NOAA P3 Radars*

The NOAA P3 tail (TA) radar is an X-band airborne Doppler radar that scans in a cone  $20^\circ$  fore and aft of the plane perpendicular to the aircraft with a scan rate of 10 rpm and along-track sampling of fore/aft sweeps of  $\sim 1.6 \text{ km}$  (Gamache et al. 1995). Retrievals of the three-dimensional wind vector are performed using the variational methodology outlined in Gamache (1997) and Reasor et al. (2009) at a grid spacing of 2 km in the horizontal and 0.5 km in the vertical. Quality control procedures on the raw observations of reflectivity and radial velocity can be found in Gamache et al. (2005). The mean storm motion vector averaged over the aircraft-sampling period was removed from the TA derived horizontal winds.

The NOAA P3 aircraft also carries a C-band Lower Fuselage (LF) radar that provides a scan of radar reflectivity every 30 seconds at approximately the flight-level height. This data is useful for identifying and tracking vortex and convective scale features of TCs close to the aircraft. The large vertical beamwidth of  $4.1^\circ$  can cause smearing of features and inadequate beam filling for ranges greater than  $\sim 60 \text{ km}$  (Marks 1985). Analysis of the LF data is confined to ranges less than 50 km to avoid these problems.

#### *c. HAMSR*

The High-Altitude Mimic Sounding Radiometer (HAMSR) is a passive microwave sounder measuring upwelling radiation from the atmosphere at frequencies sensitive to



temperature ( $\sim 50$  GHz and  $\sim 118$  GHz) and water vapor ( $\sim 183$  GHz). The intensity of convective clouds can also be estimated in regions where upwelling radiation is scattered out of the beam by ice particles, which results in anomalously low brightness temperatures (Tbs) at the instrument receiver. The HAMSR instrument scans  $\pm 60^\circ$  across-track providing a swath width of  $\sim 65$  km from the height of the GH aircraft. However, we focus on data at  $\pm 45^\circ$  because larger errors are found beyond this range (Brown et al. 2011). The footprint of HAMSR at nadir from the GH altitude is  $\sim 2$  km with an increase in size as the instrument scans off-nadir. The along-track sampling of HAMSR measurements is  $\sim 250$  m. In this study, the HAMSR Tbs are mapped to a grid with 1 km spacing to match the HIWRAP wind retrievals. The vertical resolution of the HAMSR data is dictated by each channel's weighting function, which amounts to  $\sim 2 - 3$  km intervals in height. More detailed information on HAMSR can be found in Brown et al. (2011).

### 3. Overview of Hurricane Karl

During the summer of 2010, NASA conducted the GRIP field experiment in the Atlantic Ocean basin to study the physical processes controlling hurricane formation and intensity change. A total of three NASA aircraft were deployed during GRIP with instruments onboard to measure properties of the hurricane environment and inner-core region. In this study, we focus on the inner-core aircraft (GH) and instruments (HIWRAP and HAMSR) described in the previous section. Further information about GRIP can be found in Braun et al. (2013).

Hurricane Karl began from a combination of a tropical wave moving off the African coast and an elongated trough of low pressure situated over the southwestern North

Atlantic Ocean. Figure 1 shows the best track of Karl and intensity classifications starting at 0000 UTC 14 September. Over several days time, deep convection located near the wave axis became more organized and by 1200 UTC 14 September a tropical depression formed in the northwestern Caribbean Sea (Stewart 2010). Not long after, Karl intensified to a tropical storm and made landfall on 15 September on the Yucatan Peninsula with surface winds of  $\sim 27 \text{ m s}^{-1}$ . Karl weakened while crossing land, but was able to maintain tropical storm classification ( $\sim 20 \text{ m s}^{-1}$  surface winds) with a well-organized circulation.

After emerging into the Bay of Campeche, Karl rapidly intensified from a  $\sim 20 \text{ m s}^{-1}$  tropical storm on 0600 UTC 16 September to a  $\sim 57 \text{ m s}^{-1}$  hurricane on 1200 UTC 17 September (Fig. 1). This equates to a  $\sim 37 \text{ m s}^{-1}$  increase in surface winds in a 30 h period, which is more than double the typical RI rate of  $\sim 15 \text{ m s}^{-1}$  in 24 h (Stewart 2010). Our focus in this study is the inner-core structure and dynamics during this RI episode that was sampled by the GH aircraft between  $\sim 1900$  UTC 16 September and  $\sim 0800$  UTC 17 September (see Fig. 1).

From an environmental perspective, Karl was primed for RI with high sea-surface temperatures of  $\sim 30^\circ \text{ C}$  in the Bay of Campeche, relatively low vertical wind shear of  $\sim 5 \text{ m s}^{-1}$  with the vector pointing mostly towards the southwest over the RI interval, and moist mid-level air. The large-scale vertical wind shear impacting the storm was determined from CIMSS satellite analyses and verified using NCEP re-analysis data.

#### **4. Convective burst remote sensing observations**

##### *a. Satellite evolution*

Animations of GOES IR satellite data indicate that localized convective bursts in Karl were actively pulsing for a  $\sim 12$  h period between 1200 UTC 16 September and 0000 UTC 17 September. After this time period, the convective forcing is less frequent and a more axisymmetric presentation of the cloud field emerges.

Figure 2 shows a sequence of GOES IR images of Karl spanning the period of GH observations during the storm's RI. The GOES IR data has a resolution of  $\sim 4$  km. On 1845 UTC 16 September (Fig. 2a), a region of asymmetric cold cloud tops ( $\sim -80^\circ$  C) associated with a pulsing convective burst is located in the downshear to downshear-left portions of the storm. No apparent eye is visible at this time due to the presence of heavy cloud. At 2215 UTC (Fig. 2b), the convective burst episode is still evident in the IR imagery with deep convection located in the downshear-left sector of the storm and the appearance of a cloud filled eye. A few hours later at 0140 UTC 17 September (Fig. 2c), the cold cloud top region has wrapped around to the upshear quadrants of the storm. A clearer depiction of an eye is present at this time although it is still not cloud free. Towards the end of the aircraft observation period at 0501 UTC (Fig. 2d), the cold cloud tops have diminished and spread around the storm in a more axisymmetric pattern along with the development of a large, clear eye. Karl is nearing landfall at this point, but the core region of the storm is still well offshore.

The satellite presentation of Karl's RI with localized convective bursts pulsing in the downshear quadrants of the storm, their rotation and dissipation into the upshear quadrants and development of an axisymmetric cloud structure with a clear eye at late times is common (e.g. Reasor et al. 2009; Guimond et al. 2010; Stevenson et al. 2014). In addition, the presence of lightning associated with convective bursts has become more

commonly recognized. Rinehart et al. (2014) analyzed satellite data and several GRIP datasets and found that some of the more intense convective burst activity in Karl produced significant lightning.

*b. HIWRAP time-averaged structure*

The spatial and temporal evolution of convective bursts is very turbulent in nature and requires high-resolution aircraft measurements to accurately describe their structure. A time-averaged view of the storm from HIWRAP radar measurements is first presented and then individual overpasses are analyzed from several data sources to highlight the detailed structure of convective bursts during the pulsing phase. Finally, we briefly show the structure of the vortex during the axisymmetric response phase.

Figure 3a shows HIWRAP Ku-band reflectivity overlaid with horizontal wind vectors at 2 km height on a storm-relative grid averaged over the entire GH sampling interval (~ 1900 UTC 16 September - 0800 UTC 17 September). A broad cyclonic circulation is evident with a reflectivity filled eye, which is weighted towards early time periods. There are gaps in the azimuthal coverage of the storm due to the small swath width of HIWRAP. These gaps decrease towards the storm center where estimates of the low wavenumber components of the flow are best suited.

Figure 3b shows the horizontal wind speeds at 2 km height averaged over the same time interval. The strongest winds are generally located in the downshear quadrants of the storm with large patches of  $\sim 40 - 45 \text{ m s}^{-1}$  winds in this region. The time and azimuthally averaged RMW at this level is 20 – 25 km. An interesting feature appearing in the data is the presence of small clusters of anomalously large wind speeds in the eyewall (two examples are labeled with white arrows in Fig. 3b). These clusters have a

length scale of  $\sim 10$  km and are found most notably in the downshear direction and downshear-left quadrant just inside the RMW.

Figure 4a is similar to Fig. 3a only at 8 km height centered on the inner 50 km of the storm. At this higher level, the presence of convective bursts shown by the high reflectivity anomalies between  $\sim 25 - 40$  dBZ are evident. These bursts are occurring in the downshear to downshear-left portions of the storm with evidence of rotation into the upshear quadrants. This structure is consistent with the satellite data shown in Fig. 2, only the HIWRAP data is much higher resolution and individual convective elements are discernable. The majority of the burst activity over this time interval is located inside the low-level (2 km) RMW, which is consistent with the intensifying TC composite of Rogers et al. (2013). The patches of anomalously large wind speeds shown in Fig. 3b are well correlated with the high reflectivity anomalies in Fig. 4a, which *suggests the connection of the convective bursts to the localized spin-up of the low-level wind field.* The association of the high reflectivity anomalies aloft to the localized low-level wind spin-up is burdened by the 12 – 13 h time-averaged perspective. However, individual overpasses were analyzed and they confirmed the existence of this relationship.

Figure 4b shows the horizontal wind speeds at 8 km height, which reveals similar cellular structures as the 2 km wind speeds albeit with generally reduced magnitudes. The strongest wind speeds of  $\sim 35 - 40$  m s<sup>-1</sup> are found in the downshear-left quadrant and the northeast, upshear quadrant at 8 km height. This shows that the enhanced winds associated with the convective bursts extend through a deep layer with the downshear-left quadrant containing the most intense winds.

*c. Airborne radar and radiometer analysis during the burst pulsing phase*

1) 1<sup>ST</sup> SAMPLING PERIOD (~ 1830 – 1920 UTC 16 SEPTEMBER)

The NOAA P3 aircraft sampled the RI of Karl at certain similar time periods as the NASA GH, which allows a more comprehensive study of the inner-core processes due to the large swath width of the P3 measurements. The P3 first crossed the storm center at ~ 1842 UTC 16 September. The LF radar reflectivity at flight level (3.7 km height) along with the TA radar derived wind vectors are shown in Fig. 5a at this time.

An interesting wavenumber-5 polygon structure is apparent at the eye/eyewall interface in the LF reflectivity, which is indicative of the presence of mesovortices at the locations of the vertices. The study of Hendricks et al. (2012) observed similar reflectivity structures in the rapid intensification of Hurricane Dolly (2008). The formation of mesovortices has been linked to dynamic instability in the eyewall where thin rings of potential vorticity support the phase locking and exponential growth of counter-propagating vortex Rossby waves (e.g. Schubert et al. 1999; Kossin and Schubert 2001; Rozoff et al. 2009; Hendricks et al. 2014). The above studies showed that development of mesovortices is an effective means of turbulent mixing between the eye and eyewall, which can lead to important consequences for the intensity of the hurricane.

The wind vectors in Fig. 5a show that the strongest winds ( $\sim 40 \text{ m s}^{-1}$ ) are located in the upshear (northeast) quadrant at this time and level (4 km height), which is more consistent with the time-averaged HIWRAP data at 8 km height (Fig. 4b) than at 2 km height (Fig. 3b). Figure 5b highlights the 1 – 4 km mean radial component of the flow for this transect along with perturbation wind vectors (computed by removing the azimuthal mean radial and tangential winds from the total flow and projecting back to Cartesian space) averaged over the same height interval. The analysis in Fig. 5b shows a

significant region of outflow emerging from the eye and entering the southern eyewall (see thick arrow in Fig. 5b) where an intense band of  $\sim 40$  dBZ echoes are observed (Fig. 5a). The outflow from the eye likely brings warm anomaly air into the eyewall, which helps to stimulate convection through buoyancy effects.

A broad region of inflow located radially outside the outflow feature (see thin arrow in southern half of Fig. 5b) enables kinematic convergence to help develop and sustain the intense convection in the southern eyewall as well. This convergence signature is vertically coherent down to 1 km height, which was validated by computing the divergence field (not shown). In the northwestern portion of the eyewall, a wide inflow region (see thick arrow in Fig. 5b) with peak magnitudes of  $\sim -8 \text{ m s}^{-1}$  is transporting air across the eye-eyewall interface. The perturbation wind vectors show that a cyclonic/anti-cyclonic mesovortex couplet is responsible for the transport of air across the eye-eyewall interface on the northwestern side extending down across the southern side.

Figure 6a shows HAMSR 54 GHz Tbs overlaid with HIWRAP computed horizontal wind vectors from the first GH overpass of Karl between 1853 – 1919 UTC 16 September. The aircraft crossed the storm center at  $\sim 1910$  UTC, which is  $\sim 25$  minutes after the P3 transect shown in Fig. 5. The data is shown at 2 km height, which is where the HAMSR 54 GHz weighting function peaks, assuming a standard atmosphere. The presence of light precipitation in the eye of Karl at this time allows the flow in the eye and its interaction with the eyewall to be analyzed.

In this pass, the warm anomaly of Karl is evident shown by the anomalously large Tbs in the core of the storm. For this analysis we are not as interested in the quantitative

properties of the warm core as our focus is on the qualitative structure of this feature. The eyewall of Karl with embedded convective bursts is seen by the depressed Tbs in the southern half of Fig. 6a with an intense cell located in the eastern half of the southern eyewall, which is in the downshear-left quadrant. The azimuthal mean RMW at this time and height is  $\sim 30$  km, which places the cell inside the RMW. The winds in this region are  $30 - 40 \text{ m s}^{-1}$  as computed from HIWRAP data.

An interesting feature of the HAMSR data is a finger-like protrusion of the warm core sticking out of the southern eyewall and adjacent to the most intense convective activity (labeled with white arrows in Fig. 6a). The HIWRAP winds follow this feature well and show  $10 - 20 \text{ m s}^{-1}$  flow originating in the eye and cyclonically rotating towards the intense convective cell in the eastern half of the southern eyewall. The winds from this warm anomaly protrusion show a convergence signature with the intense convective cell.

Figure 6b shows Ku band reflectivity from HIWRAP along with horizontal wind vectors for the same overpass as in Fig. 6a. The warm core protrusion observed in the HAMSR data can also be seen in the HIWRAP data through reduced reflectivity in the southern eyewall from values of  $35 - 40 \text{ dBZ}$  to  $\sim 20 \text{ dBZ}$ . *It appears that turbulent mixing between the warm, dry air in the eye with the eyewall is helping to carve out and develop the eye of Karl.* In addition to the HIWRAP winds in Fig. 6, the LF reflectivity structure (Fig. 5a) and TA perturbation winds (Fig. 5b) observed  $\sim 25$  minutes earlier show that the turbulent mixing is a result of mesovortices located near the eye/eyewall interface. Small patches of reduced reflectivity (Fig. 6b) in the same locations as the low TBs in Fig. 6a are the result of attenuation of the HIWRAP Ku band signal from the convective bursts.



Figure 7 shows nadir cross-sections of HIWRAP data for the first GH overpass (see Fig. 6). This cross-section is straight through the storm center in the north-to-south direction. Figure 7a shows Ku band reflectivity through the convective burst in the southern eyewall revealing a deep column of high values reaching  $\sim 35$  dBZ at 12 km height (x-axis  $\sim -25$  km). There is a large region of lower reflectivity ( $\sim 20$  dBZ) filling the eye that appears connected with the convective burst in the southern eyewall. In the eye region, there is a deep layer (1 – 10 km) of outflow with magnitudes of  $\sim 10 - 15 \text{ m s}^{-1}$  (Fig. 7b, x-axis  $\sim -15$  km), which is consistent with the warm core mixing into the eyewall shown in Fig. 6a at 2 km height. The outflow from the eye converges with inflowing air, located radially outside the convection, at low-to-mid levels in the core of the burst (see gray arrows in Fig. 7b). *This data indicates that the formation/maintenance of the convective burst in the southern eyewall (downshear-left quadrant) is driven by a combination of buoyancy (inferred from Fig. 6a) and horizontal, kinematic convergence (Fig. 7b). Both of these mechanisms are facilitated by the turbulent mixing of air, originating in the anomalously warm eye, with inflowing air in the low-to-mid level eyewall.* In the northern part of the eyewall in Fig. 7b, the radial flow reflects traditional azimuthal mean behavior with inflow at low levels and outflow aloft.

A significant region of descent with peak values of  $\sim -3 \text{ m s}^{-1}$  is located in the eye of Karl (wide gray arrow in Fig. 7c), which should be helping to clear and warm the eye. This descent appears to be induced by the convective updraft (thin gray arrow in Fig. 7c) occurring on the inner edge of the eyewall (x-axis  $\sim -15$  km). A reasonably strong updraft of  $\sim 10 \text{ m s}^{-1}$  (Fig. 7c) in the core of the deep convection (x-axis  $\sim -25$  km) is coincident with an anomalously large patch of cyclonic vorticity (Fig. 7d) at  $\sim 7$  km

height. Note that vorticity values are removed above 10 km height because the swath width of the HIWRAP data at these levels is very small, which places the swath edges close to nadir. The computed horizontal winds at the swath edges have larger uncertainty due to the HIWRAP scanning geometry (Guimond et al. 2014). At low levels on the inner edge of the deep convection (x-axis  $\sim -18$  km), a weak-moderate updraft (Fig. 7c) is collocated with an intense cyclonic vorticity anomaly with values of  $10^{-2} \text{ s}^{-1}$  (Fig. 7d).

These observations suggest that the convective burst sampled here is rapidly rotating through a deep layer as has been observed in previous studies (e.g. Reasor et al. 2005; Houze et al. 2009). For a mature TC such as Karl, the production of vorticity is likely dominated by the stretching of pre-existing cyclonic vorticity in the eyewall (e.g. Montgomery et al. 2006). In the northern portion of the eyewall, an elevated band of cyclonic vorticity that tilts outward with height is observed (Fig. 7d), which fits more closely with typical azimuthal mean TC structure.

## 2) 2<sup>nd</sup> SAMPLING PERIOD ( $\sim 1920 - 2000$ UTC 16 SEPTEMBER)

Approximately 20 minutes after the first GH overpass, the NOAA P3 aircraft penetrated the core of Karl again with a center crossing at  $\sim 1930$  UTC 16 September. Figure 8a shows LF radar reflectivity at flight level (3.6 km height) along with the TA radar derived wind vectors at 4 km height. Intense reflectivity between 45 – 50 dBZ is present on the western half of the storm while the eastern half is ragged without a continuous region of elevated reflectivity. Significant reflectivity is located in the eye of the storm and animations of several LF scans show mesovortex-like features mixing into the eye from the eyewall. Much like the previous transect, the strongest winds are located in the northeast (upshear) quadrant.

Figure 8b shows the perturbation wind vectors, averaged over the 1 – 4 km height interval, overlaid on the mean divergence field in this same layer. A wavenumber-2 divergence pattern is observed with strong regions of convergence in the western and eastern portions of the eyewall. The convergence region in the western eyewall (downshear quadrants) is consistent with the intense reflectivity band (Fig. 8a), while the eastern eyewall (upshear quadrants) is having difficulty developing perhaps as a result of the vertical wind shear. The perturbation wind vectors reveal a similar cyclonic/anti-cyclonic mesovortex couplet as the previous transect (Fig. 5b) although a data gap in the southwestern quadrant in Fig. 8b makes the placement of the anti-cyclonic circulation rather broad and with some uncertainty. The counter-rotating circulations are consistent with the divergence signatures and are directing air across the eye-eyewall interface with inflow to the eye on the western side and outflow to the eyewall on the eastern side.

Figure 9 is similar to Fig. 6a only for the second GH overpass of Karl between 1938 – 1957 UTC 16 September. This is a diagonal pass from southeast to northwest, which covers part of the upshear left quadrant of the storm where depressed Tbs from HAMSR show the straining/elongation of deep convection by the advective tendencies of the cyclonic flow. The maximum HIWRAP winds at 2 km height are  $\sim 50 \text{ m s}^{-1}$  in the northwest eyewall and  $\sim 30 \text{ m s}^{-1}$  in the southeast eyewall where the flow has a radially outward directed component into the convection. The warmest Tbs are located on the northwestern side of the eye.

The vertical structure of HIWRAP Ku band reflectivity at nadir for this overpass is shown in Fig. 10a. Deep convection with similar vertical structure and radial location to that shown in the previous GH overpass (Fig. 7a) is observed in the southeastern (upshear

left) portion of the eyewall with significant reflectivity filling the eye adjacent to this cell. The northwest portion of the eyewall is not as convectively active and the eye is clear adjacent to this side of the eyewall, which is consistent with the previous overpass and the warmest Tbs shown in Fig. 9.

Figure 10b shows the radial wind speeds for this overpass. The dominant features are a region of midlevel inflow located radially outside the convective burst and a deep column of strong outflow that traverses the eye region and enters the core of the burst (see gray arrows). These winds acquire entropy from the warm anomaly eye (see Fig. 9) likely leading to assistance in convective development in the southeastern eyewall through buoyancy effects. The flow across the eye is similar to that observed by the P3 shown in Fig. 8b and is driven by the counter-rotating mesovortex circulations. On the northwestern side of the storm, low-level inflow and mid-level outflow resembles azimuthal mean hurricane structure.

The vertical motion structure in Fig. 10c shows a broad region of descent in the eye adjacent to the convective burst with values of  $\sim -2 - -4 \text{ m s}^{-1}$ . This descent appears to be generated by the convective activity through compensating motions around convective updrafts (see gray arrows). The broad region of forced descent in the eye is similar to that observed in the previous overpass in the downshear-left quadrant. This robust structure should lead to a drying and warming effect over time, which will be demonstrated with the data in subsequent overpasses.

Finally, instead of showing the vorticity for this overpass, which was somewhat similar to the previous transect, the tangential winds are presented in Fig. 10d. The tangential winds are  $\sim 20 \text{ m s}^{-1}$  stronger in the northwest eyewall up to midlevel regions

with peak values of  $\sim 50 \text{ m s}^{-1}$  at low levels. In the deep convection, large tangential wind speeds are located at high levels (12 – 13 km), which is due to strong updrafts transporting high angular momentum air aloft. It appears the convective towers are trying to build a deeper, more intense vortex in this portion of the eyewall.

### 3) 3<sup>rd</sup> SAMPLING PERIOD ( $\sim 2030 - 2100$ UTC 16 SEPTEMBER)

The NOAA P3 tracked through the center of Karl one last time centered at 2042 UTC 16 September. Figure 11a shows the LF reflectivity at flight level (3.6 km) along with TA derived wind vectors at 4 km height for this transect. The western eyewall continues to be the dominant feature with a large region of reflectivity at or above 50 dBZ. An animation of several LF scans within  $\pm 2$  minutes of the one shown in Fig. 11a indicates that the western eyewall with embedded deep convective towers is intensifying rapidly (in terms of reflectivity) during the P3 penetration of the core. The horizontal winds in this region are  $\sim 10 \text{ m s}^{-1}$  stronger than those from the previous P3 sampling  $\sim 1$  hour earlier at 1930 UTC (see Fig. 8a). The eastern eyewall is still ragged without a coherent eyewall apparent in the reflectivity, while the southern eyewall has increased banding features, which appear to be coalescing.

The divergence field for this flight averaged over the 1 – 4 km layer is shown in Fig. 11b with 1 – 4 km height averaged perturbation winds overlaid. The cyclonic/anti-cyclonic mesovortex couplet identified in the previous P3 penetrations continues to persist two hours after initial diagnosis. At this time period, the mesovortex couplet has rotated cyclonically with the mean flow placing the cyclonic circulation directly North of the anti-cyclonic circulation in the western eyewall. These circulations are consistent with a strong region of convergence in the western eyewall, which is helping to develop

the convective bursts, and a west-to-east flow across the eye. In the eastern eyewall, which is not well defined in the LF reflectivity, another small-scale cyclonic circulation is evident in the perturbation wind vectors. This circulation is helping to direct a southerly flow across portions of the eastern eye-eyewall interface.

The next GH overpass of Karl sampled directly along the shear vector with a southwest to northeast transect just north of the storm center at ~ 2040 UTC 16 September, which is ~ 2 minutes behind the P3. Figure 12 shows HAMSR 54 GHz Tbs along with HIWRAP horizontal wind vectors at 2 km height for this overpass. A very intense convective cell located in the down-shear direction is present in the HAMSR data with Tbs falling well below 200 K (strong ice scattering) in the core of the ~ 10 km wide feature. This cell is located at and just inside the azimuthally averaged RMW at this level.

In the eye of the storm, the HIWRAP winds reveal a cyclonic mesovortex circulation that is directing air out of the northern portion of the eye and into the convective burst. The HAMSR data shows that the air being transported into the burst is anomalously warm with Tbs significantly larger than ambient values. The mesovortex circulation identified in the HIWRAP data is also seen at the same location in the TA perturbation wind vectors (see Fig. 11b).

The close coordination of the GH and P3 aircraft during this time allows a comparison of the storm structure from the HIWRAP and TA radars. The appendix also shows error statistics between HIWRAP computed winds and P3 flight level data. Figure 13a shows HIWRAP Ku band reflectivity in a vertical cross section averaged between ~ 0 – 6 km in the +y direction (see Fig. 12 for averaging domain) while Fig. 13b shows the

537 same field only for the TA X band data. Both radars show similar qualitative structures  
538 with a deep convective cell and elevated reflectivity to  $\sim 15$  km height in the downshear  
539 eyewall of Karl. However, the quantitative structure of this cell differs to some extent  
540 with HIWRAP revealing a more intense, concentrated reflectivity signature while the P3  
541 TA radar shows a weaker and more diffuse cell.

542 These differences are due to several things: the higher resolution (sampling) of the  
543 HIWRAP radar, the use of a Gaussian distance-weighted interpolation in the TA data,  
544 calibration biases with both radars and rapid evolution of the convection over the  $\sim 2$   
545 minute sampling offset. The smoothing in the interpolation used to produce the gridded  
546 TA data plays a significant role in the reflectivity differences. A higher resolution TA  
547 product that minimizes smoothing was also analyzed and showed increases in reflectivity  
548 magnitudes of  $\sim 5 - 10$  dBZ (not shown), which are more similar to HIWRAP.  
549 Unfortunately, this product is only available in a vertical slice along the aircraft track,  
550 which prevents the presentation of the mean structure of the inner core shown in Fig. 13  
551 and subsequent figures. Therefore, we proceed with the default TA dataset.

552 The radial winds from HIWRAP (Fig. 14a) show a strong convergence signature  
553 (divergence field was computed, but not shown) directly below the intense convective  
554 cell with outflow of  $\sim 5 - 8$  m s<sup>-1</sup> crossing the eye-eyewall interface. This outflow from  
555 the eye brings warm anomaly air into the eyewall helping to fuel the convective cell as  
556 was shown in Fig. 12. The TA radar radial winds (Fig. 14b) show similar features in  
557 similar locations, but the intensity of the flow is reduced. The higher resolution TA  
558 product agrees more closely with HIWRAP.

A deep column (1 – 12 km) of inflow ( $\sim -5 - -10 \text{ m s}^{-1}$ ) coincident with the convective cell is present in the HIWRAP data (Fig. 14a) and in the TA data at low and high levels (Fig. 14b), which acts to locally spin-up the tangential winds through the inward transport of high angular momentum air. The proximity of the cell to the center of circulation (inside RMW of  $\sim 23 \text{ km}$ ) also allows strong projection onto the azimuthal mean dynamics.

Figure 15a shows the HIWRAP derived vertical winds in the downshear eyewall for this same averaged section of data. A deep updraft is present in the core of the convective cell with a strong pulse approaching  $10 \text{ m s}^{-1}$  located above 10 km height. A downdraft of  $\sim -3 \text{ m s}^{-1}$  is located on the inner edge of the eyewall (see gray arrow), which is likely formed through mass conserving motions around the strong updraft. The TA vertical winds in Fig. 15b show similar structure to that from HIWRAP with a deep, wide updraft maximized at  $\sim 10 \text{ km}$  height, but again with reduced magnitudes. The TA data also shows compensating downdrafts on either side of the updraft with a broad region of descent ( $\sim -1 - -2 \text{ m s}^{-1}$ ) located radially inward of the cell (see gray arrow). This broad descent is well positioned to dry and warm the eye as observed in previous overpasses (see Fig. 7c and Fig. 10c). This is also true of the HIWRAP observed inner-edge downdraft and is a common feature around convective towers located in the eyewall of intensifying TCs (e.g. Heymsfield et al. 2001; Guimond et al. 2010).

#### *d. HIWRAP data analysis during the vortex response phase*

The main advantage of the GH aircraft is the long duration sampling, which allows continued analysis of the RI of Karl when the P3 aircraft returned to base following the 2042 UTC 16 September eye penetration. The GOES IR satellite data analyzed in



section 4a showed that the majority of the convective burst activity was finished by ~ 0000 UTC 17 September. After this time, the vortex went through a response phase that included axisymmetrization of the convective anomalies, which was sampled by the GH aircraft for a period of ~ 8 h.

Figure 16 shows vertical cross sections of HIWRAP Ku band reflectivity and tangential wind speed at nadir for a series of overpasses of the inner-core of Karl spanning this 8 h period. At 0012 UTC 17 September (Fig. 16a), the vertical structure of the eye/eyewall already looks different than that shown for the burst pulsing phase (e.g. Fig. 7a and Fig. 10a). There is little reflectivity filling the eye, and the beginning of a more sloped structure to the eyewall is observed. The tangential winds peak at ~ 40 m s<sup>-1</sup> in the southeast quadrant and ~ 45 m s<sup>-1</sup> in the northwest quadrant with both sides showing contours sloping outward with height. About 3.5 h later at 0345 UTC (Fig. 16b), the axisymmetric structure reflected in the cross-section continues to develop with significant sloping of the eyewall reflectivity and tangential winds with height. The eye has also widened, which is indicative of increased subsidence and growth of the warm core (backed by HAMS data; not shown) in association with an enhanced secondary circulation from the vortex response to the convective forcing.

Over the next ~ 4 h, the trend towards a wider, clearer and warmer eye with a sloping eyewall structure reminiscent of axisymmetric hurricanes continues to prevail (Figs. 16c and 16d), except for the presence of a transient convective burst in the northwest eyewall in Fig. 16c.

## 5. Conclusions

In this paper, the evolution of rapidly intensifying Hurricane Karl (2010) is examined from a suite of remote sensing observations during the NASA Genesis and Rapid Intensification (GRIP) field experiment. The novelties of this study are in the analysis of data from a new airborne Doppler radar (HIWRAP) and a new airborne platform (NASA Global Hawk) for hurricane research that allows long endurance sampling (up to 24 h). Supporting data from a microwave sounder (HAMSR) coincident with HIWRAP and coordinated flights with the NOAA WP-3D aircraft carrying the lower fuselage (LF) and Tail (TA) radars help to provide a detailed analysis of the storm. The focus of the analysis is on documenting and understanding the structure, evolution and role of small scale, deep convective forcing in the storm intensification process.

After Karl emerged off the Yucatan Peninsula as a tropical storm, satellite data revealed the presence of deep convective bursts located primarily in the downshear to downshear-left quadrants of the storm. The bursts went through a  $\sim 12$  h pulsing phase followed by a vortex response phase that included axisymmetrization of the convective anomalies and the development of a wide, clear eye. During the time period of the burst pulsing and vortex response phase, the surface wind speeds in Karl increased by  $\sim 37$  m  $s^{-1}$  in a 30 h period, which is more than double the typical rapid intensification rate of  $\sim 15$  m  $s^{-1}$  in 24 h (Stewart 2010).

The Global Hawk (GH) and P3 aircraft data was analyzed from  $\sim 1900$  UTC 16 September – 0800 UTC 17 September, which covered portions of the convective burst pulsing phase and vortex response phase. The aircraft remote sensing data and analysis indicates the following science results.

The convective bursts formed primarily in the downshear to downshear-left quadrants through a combination of two main processes: (1) convergence generated from counter-rotating mesovortex circulations and the larger scale flow and (2) the turbulent transport of warm, buoyant air from the eye to the eyewall at low-to-mid levels. Reflectivity snapshots and animations from the LF radar showed a distinct wavenumber-5 structure at the eye/eyewall interface and movement of small-scale features in the eye and across the interface during the aircraft-sampling period. These structures and the observed turbulent mesovortex circulations that produce significant eye-eyewall mixing form as a result of dynamic instability in the axisymmetric vortex (e.g. Schubert et al. 1999; Kossin and Schubert 2001; Rozoff et al. 2009; Hendricks et al. 2012).

Horizontal wind fields computed from the TA and HIWRAP measurements showed that the mesovortex circulations were primarily located in the western and southern (downshear) eye/eyewall region where the most intense convective activity was found. In one GH overpass, a finger-like protrusion of the warm core observed from HAMSRR was observed to rotate cyclonically into the eyewall, likely helping to fuel convective towers observed in this region. The array of mesoscale circulations and convective bursts rotated cyclonically with the mean flow over time. As the bursts rotated into the upshear quadrants, they were influenced by an across eye flow induced by the counter-rotating mesovortex circulations. Figure 17 shows a conceptual diagram summarizing the remote sensing measurements and the analysis of the mesoscale dynamics described above.

The mechanism for convective burst formation identified in the observations is similar to that determined by Braun et al. (2006) using a numerical simulation of Hurricane Bonnie (1998). In this study, the initiation of updraft towers was found to

result from convergence between shear induced asymmetries and the cyclonic flow associated with eyewall mesovortices. Reasor et al. (2009) also found observational evidence for the triggering of convective bursts through the interaction of low-level environmental flow and low-wavenumber vorticity asymmetries in the eyewall of Hurricane Guillermo (1997). The HIWRAP and P3 TA radar analysis described in this paper highlights a similar convergence mechanism with the addition of significant transport of warm, buoyant air from the eye into the eyewall as indicated by the HIWRAP and HAMSR data. This additional piece of evidence linked to the formation and/or maintenance of the convective bursts is supported by the trajectory analysis of a numerically simulated hurricane by Cram et al. (2007).

The formation of a clear eye and growth of the warm core of Karl are influenced by both asymmetric and axisymmetric processes. The TA and especially HIWRAP data showed that convective induced descent on the inner-edge of the eyewall and in the eye itself was significant, which helps to warm and dry the eye over time. In addition, in one GH overpass the HIWRAP and HAMSR data revealed that turbulent mixing between the eye and eyewall eroded the reflectivity on a local scale. These processes contribute largely to an asymmetric development of the eye and warm core of Karl. During the vortex response phase where the convective bursts are less pronounced and axisymmetrization of the convective anomalies is dominant, the development of the eye has a clear axisymmetric signal shown by the time series of HIWRAP data.

Taking in the full scope of the data and analysis, we conclude that the convective bursts played an important role in the rapid intensification of Hurricane Karl (2010). These results build on a large body of evidence supporting the role of convective bursts

and their axisymmetric and asymmetric dynamical pathways to the TC intensification problem. We also note that the routine use of the Global Hawk aircraft carrying the HIWRAP and HAMSR instruments for the study of TC evolution and operational forecasting in the future appears promising if the function of the aircraft can mirror that conducted during GRIP.

*Acknowledgments.* We would like to thank Dr. Lihua Li, Matt McLinden, Martin Perrine and Jaime Cervantes for their engineering efforts on HIWRAP during GRIP. We also thank the JPL HAMSR team for providing level 1B data used in this study, which was obtained from the NASA Global Hydrology Resource Center in Huntsville, Alabama. Discussions with Dr. Scott Braun were useful and helped to clarify the presentation of the data. Dr. Lin Tian helped with early HIWRAP data processing. The NASA GRIP and HS3 field programs supported this research. The NASA weather program under Dr. Ramesh Kakar supported GRIP. The first author was also partially supported by the Institute of Geophysics and Planetary Physics (IGPP) at Los Alamos National Laboratory. The first author thanks Robert Kilgore for his artistic work on the conceptual diagram.

## APPENDIX

### **Comparison of HIWRAP wind retrievals to flight level data**

The HIWRAP radar participated in the NASA Hurricane and Severe Storm Sentinel (HS3) field campaign between the years 2012 – 2014 to study hurricane evolution. As part of this experiment, a coordinated flight between the Global Hawk and the NOAA P3

aircraft on September 25, 2013 allowed for the opportunity to validate the HIWRAP wind retrievals with flight level wind data. The aircraft sampled the end of a large-scale frontal system with a mix of stratiform and weak convective precipitation.

To make the comparisons, all HIWRAP data with a time offset of  $< 10$  minutes and space offset of  $< 1$  km from the P3 aircraft and with reflectivity  $> 5$  dBZ are retained. These data are then interpolated to the locations of the flight level measurements (height of  $\sim 2$  km). In an attempt to match the along-track sampling of the flight level winds (1 Hz or  $\sim 100 - 150$  m for a typical P3 airspeed) with the HIWRAP wind retrieval grid (1 km) a 10-point running mean filter is applied to the flight level winds.

Figure A1 shows a scatter plot of the horizontal wind speed error, defined as  $|\text{HIWRAP} - \text{P3 flight level}|$ , vs. the flight level horizontal wind speed. In this figure, HIWRAP Ku band data is shown. There is a clear trend of lower errors for higher wind speeds. For all the points in Fig. A1 ( $N = 2727$ ) the RMSE for wind speed and direction (not shown) is  $7.8 \text{ m s}^{-1}$  and  $27^\circ$ , respectively. When considering points where the wind speed is  $> 10 \text{ m s}^{-1}$  ( $N = 1077$ ) the RMSE for wind speed and direction is  $1.3 \text{ m s}^{-1}$  and  $19^\circ$ , respectively. These errors are slightly lower for Ka band data likely due to the higher signal-to-noise ratios when compared to Ku band. For example, when the wind speed is  $> 10 \text{ m s}^{-1}$  ( $N = 1321$ ) the RMSE for wind speed and direction using Ka band data is  $1.1 \text{ m s}^{-1}$  and  $15^\circ$ . No clear reflectivity dependence is observed in Fig. A1, but the values give an indication of the intensity of precipitation sampled.

Coordination between the Global Hawk and NOAA P3 aircraft also occurred for one overpass of Hurricane Karl during GRIP on September 16, 2010 at  $\sim 2040$  UTC. The same procedures described above were applied to this data. The flight level

measurements were located between 3.5 and 3.8 km height and the time offset between the aircraft was  $\sim 2 - 3$  minutes. Figure A2 shows these comparison results for the same kind of scatter plot as that in Fig. A1. A trend for lower errors with increasing wind speeds is not observed with the range of values sampled here, but a slight indication of lower errors for higher reflectivity values is somewhat apparent. For all the points in Fig. A2 ( $N = 239$ ) the RMSE for wind speed and direction (not shown) is  $4.0 \text{ m s}^{-1}$  and  $11^\circ$ , respectively.

## References

- Braun, S., M. T. Montgomery, and Z. Pu, 2006: High-resolution simulation of Hurricane Bonnie (1998). Part I: The organization of eyewall vertical motion. *J. Atmos. Sci.*, **63**, 19–42.
- Braun, S., R. Kakar, E. Zipser, G. Heymsfield, C. Albers, S. Brown, S. Durden, S. Guimond, J. Halverson, A. Heymsfield, S. Ismail, B. Lambrigtsen, T. Miller, S. Tanelli, J. Thomas and J. Zawislak, 2013: NASA’s Genesis and Rapid Intensification Processes (GRIP) field experiment. *Bull. Amer. Meteor. Soc.*, **94**, 345 – 363.
- Brown, S.T., Lambrigtsen, B., Denning, R.F., Gaier, T., Kangaslahti, P., Lim, B.H., Tanabe, J.M., Tanner, A.B., 2011: The High-Altitude MMIC Sounding Radiometer for the Global Hawk Unmanned Aerial Vehicle: Instrument description and performance. *IEEE Transactions on Geoscience and Remote Sensing*, doi: 10.1109/TGRS.2011.2125973.
- Cram, T.A., J. Persing, M. T. Montgomery, and S.A. Braun, 2007: A lagrangian trajectory view on transport and mixing processes between the eye, eyewall and environment using a high-resolution simulation of Hurricane Bonnie (1998). *J. Atmos. Sci.*, **64**, 1835 – 1856.
- Emanuel, K.A., 1986: An air-sea interaction theory for tropical cyclones. Part I: Steady-



state maintenance. *J. Atmos. Sci.*, **43**, 2044-2061.

Gamache, J.F., F.D. Marks, and F. Roux, 1995: Comparison of three airborne Doppler sampling techniques with airborne in situ wind observations in Hurricane Gustav (1990). *J. Atmos. Oceanic Technol.*, **12**, 171 – 181.

Gamache, J.F., 1997: Evaluation of a fully three-dimensional variational Doppler analysis technique. Preprints, *28th Conf. on Radar Meteorology*, Austin, TX, Amer. Meteor. Soc., 422 – 423.

Gamache, J.F., 2005: Real-time dissemination of hurricane wind fields determined from airborne Doppler radar data. National Hurricane Center, 38 pp. [Available online at [http://www.nhc.noaa.gov/jht/2003-2005reports/DOPLRgamache\\_JHTfinalreport.pdf](http://www.nhc.noaa.gov/jht/2003-2005reports/DOPLRgamache_JHTfinalreport.pdf)]

Guimond, S. R., G. M. Heymsfield, and F. J. Turk, 2010: Multiscale observations of Hurricane Dennis (2005): The effects of hot towers on rapid intensification. *J. Atmos. Sci.*, **67**, 633–654.

Guimond, S.R., L. Tian, G.M. Heymsfield, and S.J. Frasier, 2014: Wind retrieval algorithms for the IWRAP and HIWRAP airborne Doppler radars with applications to hurricanes. *J. Atmos. Oceanic Technol.*, **31**, 1189 – 1215.

Guimond, S.R., J.M. Reisner, S. Marras, and F.X. Giraldo, 2016: The impacts of

788 numerical schemes on asymmetric hurricane intensification. *J. Atmos. Sci.*, submitted.

789

790 Hendricks, E.A., B.D. McNoldy, and W.H. Schubert, 2012: Observed inner-core

791 structural variability in Hurricane Dolly (2008). *Mon. Wea. Rev.*, **140**, 4066 – 4077.

792

793 Hendricks, E.A., W.H. Schubert, Y. Chen, H. Kuo and M.S. Peng, 2014: Hurricane

794 eyewall evolution in a forced shallow-water model. *J. Atmos. Sci.*, **71**, 1623 – 1643.

795

796 Heymsfield, G. M., J. B. Halverson, J. Simpson, L. Tian, and T. P. Bui, 2001: ER-2

797 Doppler radar investigations of the eyewall of Hurricane Bonnie during the

798 Convection and Moisture Experiment-3. *J. Appl. Meteor.*, **40**, 1310–1330.

799

800 Houze, R.A., W.C. Lee, and M.M. Bell, 2009: Convective contribution to the genesis of

801 Hurricane Ophelia (2005). *Mon. Wea. Rev.*, **137**, 2778 – 2800.

802

803 Kaplan, J., and M. DeMaria, 2003: Large-scale characteristics of rapidly intensifying

804 tropical cyclones in the North Atlantic basin. *Wea. Forecasting*, **18**, 1093 – 1108.

805

806 Kelley, O. A., J. Stout, and J. B. Halverson, 2004: Tall precipitation cells in tropical

807 cyclone eyewalls are associated with tropical cyclone intensification. *Geophys. Res.*

808 *Lett.*, **31**.

809

810 Kossin, J.P., and W.H. Schubert, 2001: Mesovortices, polygonal flow patterns, and rapid

811 pressure falls in hurricane-like vortices. *J. Atmos. Sci.*, **58**, 2196 – 2209.

812

813 Li, L., G.M. Heymsfield, J. Carswell, D. Schaubert, M. Mclinden, J. Creticos, M. Perrine,  
814 M. Coon, J. Cervantes, M. Vega, S. Guimond, L. Tian, and A. Emory, 2015: The  
815 NASA High-altitude Imaging Wind and Rain Airborne Profiler (HIWRAP). *IEEE*  
816 *Trans. Geosci. Remote Sens.*, **54**, 298 – 310.

817

818 Marks, F.D., 1985: Evolution and structure of precipitation in Hurricane Allen (1980).  
819 *Mon. Wea. Rev.*, **113**, 909 – 930.

820

821 Molinari, J. and D. Vollaro, 2010: Rapid Intensification of a Sheared Tropical  
822 Storm. *Mon. Wea. Rev.*, **138**, 3869–3885.

823

824 Montgomery M. T., and R. J. Kallenbach, 1997: A theory for vortex Rossby waves and  
825 its application to spiral bands and intensity changes in hurricanes. *Quart. J. Roy.*  
826 *Meteor. Soc.*, **123**, 435–465.

827

828 Montgomery, M. T., M. Nicholls, T. Cram, and A. Saunders, 2006: A vortical hot  
829 tower route to tropical cyclogenesis. *J. Atmos. Sci.*, **63**, 355–386.

830

831 Nolan, D.S., and L.D. Grasso, 2003: Three-dimensional, nonhydrostatic perturbations to  
832 balanced, hurricane-like vortices. Part II: Symmetric response and nonlinear  
833 simulations. *J. Atmos. Sci.*, **60**, 2717-2745.

834

835 Nolan, D.S., Y. Moon, and D.P. Stern, 2007: Tropical cyclone intensification from

836 asymmetric convection: Energetics and efficiency. *J. Atmos. Sci.*, **64**, 3377-3405.

837

838 Persing, J., M.T. Montgomery, J.C. McWilliams, R.K. Smith, 2013: Asymmetric and

839 axisymmetric dynamics of tropical cyclones. *Atmos. Chem. Phys.*, **13**, 12299 – 12341.

840

841 Reasor, P.D., M.T. Montgomery, F.D. Marks Jr., and J.F. Gamache, 2000: Low-

842 wavenumber structure and evolution of the hurricane inner core observed by airborne

843 dual-Doppler radar. *Mon. Wea. Rev.*, **128**, 1653 – 1680.

844

845 Reasor, P.D., M.T. Montgomery, and L.F. Bosart, 2005: Mesoscale observations of the

846 genesis of Hurricane Dolly (1996). *J. Atmos. Sci.*, **62**, 3151 – 3171.

847

848 Reasor, P. D., M. D. Eastin, and J. F. Gamache, 2009: Rapidly intensifying Hurricane

849 Guillermo (1997). Part I: Low-wavenumber structure and evolution. *Mon. Wea. Rev.*,

850 **137**, 603–631.

851

852 Rinehart, B., H. Fuelberg, R. Blaskeslee, D. Mach, A. Heymsfield, A. Bansemer, S.L.

853 Durden, S. Tanelli, G. Heymsfield, and B. Lambrigtsen, 2014: Understanding the

854 relationships between lightning, cloud microphysics, and airborne radar derived storm

855 structure during Hurricane Karl (2010). *Mon. Wea. Rev.*, **142**, 590 – 605.

856

857 Rogers, R.F., P.D. Reasor, and S. Lorsolo, 2013: Airborne Doppler observations of the  
858 inner-core structural differences between intensifying and steady-state tropical  
859 cyclones. *Mon. Wea. Rev.*, **141**, 2970 – 2991.

860

861 Rogers, R. F., P.D. Reasor, and J.A. Zhang, 2015: Multiscale structure and evolution of  
862 Hurricane Earl (2010) during rapid intensification. *Mon. Wea. Rev.*, **143**, 536 – 562.

863

864 Rotunno, R., and K.A. Emanuel, 1987: An air-sea interaction theory for tropical  
865 cyclones. Part II: Evolutionary study using a nonhydrostatic axisymmetric numerical  
866 model. *J. Atmos. Sci.*, **44**, 542-561.

867

868 Rozoff, C.M., J.P. Kossin, W.H. Schubert, and P.J. Mulero, 2009: Internal control of  
869 hurricane intensity: The dual nature of potential vorticity mixing. *J. Atmos. Sci.*, **66**,  
870 133 – 147.

871

872 Schubert, W.H., and J.J. Hack, 1982: Inertial stability and tropical cyclone development.  
873 *J. Atmos. Sci.*, **39**, 1687 – 1697.

874

875 Schubert, W.H., M.T. Montgomery, R.K. Taft, T.A. Guinn, S.R. Fulton, J.P. Kossin, and  
876 J.P. Edwards, 1999: Polygonal eyewalls, asymmetric eye contraction, and potential  
877 vorticity mixing in hurricanes. *J. Atmos. Sci.*, **56**, 1197 – 1223.

878

879 Shapiro, L.J. and H.E. Willoughby, 1982: The response of balanced hurricanes to local

sources of heat and momentum. *J. Atmos. Sci.*, **39**, 378 – 394.

Simpson, J., J. B. Halverson, B. S. Ferrier, W. A. Petersen, R. H. Simpson, R. Blakeslee, and S. L. Durden, 1998: On the role of “hot towers” in tropical cyclone formation. *Meteor. Atmos. Phys.*, **67**, 15–35.

Steranka, J., E.B. Rodgers, and R.C. Gentry, 1986: The relationship between satellite-measured convective bursts and tropical cyclone intensification. *Mon. Wea. Rev.*, **114**, 1539 – 1546.

Stevenson, S.N., K.L. Corbosiero, and J. Molinari, 2014: The convective evolution and rapid intensification of Hurricane Earl (2010). *Mon. Wea. Rev.*, **142**, 4364 – 4380.

Stewart, S., 2010: Tropical cyclone report: Hurricane Karl 14 – 18 September 2010. National Hurricane Center, 17 pp. [Available online at <http://www.nhc.noaa.gov/2010atlan.shtml>].

Willoughby, H.E., and M.B. Chelmow, 1982, Objective determination of hurricane tracks from aircraft observations. *Mon. Wea. Rev.*, **110**, 1298 – 1305.

## FIGURE CAPTIONS

1. Best track of Hurricane Karl (2010) starting from 0000 UTC 14 September with intensity classifications marked every six hours. The days in September at 0000 UTC are also shown. The green circles denote tropical depression status, open hurricane symbols are tropical storm and closed hurricane symbols are hurricane status with the category listed in the center. The inset shows the time series of maximum surface wind speed in  $\text{m s}^{-1}$  with the Global Hawk flight bracketed with the black lines.

2. A sequence of GOES IR images of Hurricane Karl (2010) in the Bay of Campeche during an RI episode spanning the GH flights into the storm. The times shown are (a) 1845 UTC 16 September, (b) 2215 UTC 16 September, (c) 0140 UTC 17 September and (d) 0501 UTC 17 September. The white arrow in (a) denotes the environmental vertical wind shear vector valid over the time interval. The star represents the estimated storm center. The track of the GH  $\pm 2$  h from the satellite time stamp is shown in white with the large numbers denoting the hour (UTC).

3. Composite analysis of HIWRAP data averaged over the total Global Hawk sampling interval (12 – 13 h) at 2 km height for (a) Ku band reflectivity (dBZ) and horizontal wind vectors and (b) horizontal wind speeds ( $\text{m s}^{-1}$ ). The white arrows in (b) highlight anomalously large wind speeds in the eyewall discussed in the text.

4. As in Fig. 3 only at 8 km height and zoomed in on the inner-core of Karl. The large, gray arrow in (a) is the large-scale vertical wind shear vector valid for this time interval

with a value of  $\sim 5 \text{ m s}^{-1}$ . The thick white arrows in (a) show the locations of low-level (2 km) anomalously large wind speeds in the eyewall (see Fig. 3b). The white circle in (a) shows the location of the low-level (2 km), time and azimuthally averaged RMW.

5. NOAA P3 flight through the inner-core of Hurricane Karl (2010) centered at  $\sim 1842$  UTC 16 September showing (a) LF C-band reflectivity at 3.7 km height overlaid with TA derived winds at 4 km height and (b) TA derived radial wind speeds averaged between 1 – 4 km height overlaid with perturbation wind vectors averaged over the same interval. The white arrows in (b) highlight features discussed in the text. The gray line in (b) marks the eye-eyewall interface using the gradient in LF reflectivity. The “C” and “A” letters in (b) denote the centers of cyclonic and anti-cyclonic mesovortex circulations, respectively.

6. Global Hawk overpass of the inner-core of Hurricane Karl (2010) between 1853 – 1919 UTC 16 September showing (a) HAMS R 54 GHz Tbs (K) and (b) HIWRAP Ku band reflectivity (dBZ). In both figures, horizontal wind vectors from HIWRAP are overlaid and the analysis level is 2 km height. The white arrows in (a) highlight a feature discussed in the text. The reference vector in (a) applies to both figures. Note that the azimuthal mean RMW at this time and level is  $\sim 30 \text{ km}$ .

7. HIWRAP vertical cross sections at nadir through the storm center in the North-South direction for the Global Hawk overpass between 1853 – 1919 UTC 16 September. The data shown is (a) Ku band reflectivity (dBZ), (b) meridional (radial) winds ( $\text{m s}^{-1}$ ), (c)



vertical winds ( $\text{m s}^{-1}$ ) and (d) vertical vorticity ( $\text{s}^{-1}$ ). The large gray arrows in (b) and (c) highlight features discussed in the text.

8. NOAA P3 flight through the inner-core of Hurricane Karl (2010) centered at  $\sim 1930$  UTC 16 September showing (a) LF reflectivity at 3.6 km height overlaid with TA derived winds at 4 km height and (b) TA derived divergence ( $\text{s}^{-1}$ ) averaged between 1 – 4 km height overlaid with perturbation winds averaged over the same interval. The gray line in (b) marks the eye-eyewall interface using the gradient in LF reflectivity. The “C” and “A” letters in (b) denote the centers of cyclonic and anti-cyclonic mesovortex circulations, respectively.

9. As in Fig. 6a, but for the GH overpass between 1938 – 1957 UTC 16 September. The large white circle denotes the azimuthally averaged RMW at 2 km height and the white dot is the storm center.

10. As in Fig. 7 except for the Global Hawk overpass between 1938 – 1957 UTC 16 September. The data shown is (a) Ku band reflectivity (dBZ), (b) radial winds ( $\text{m s}^{-1}$ ), (c) vertical winds ( $\text{m s}^{-1}$ ) and (d) tangential winds ( $\text{m s}^{-1}$ ). The gray arrows in (b) and (c) highlight features discussed in the text.

11. As in Fig. 8, only for the NOAA P3 transect centered at  $\sim 2042$  UTC 16 September.

12. As in Fig. 6a, but for the GH overpass between 2009 – 2055 UTC 16 September with a center crossing at ~ 2040 UTC. The large white circle denotes the azimuthally averaged RMW at 2 km height and the white dot is the storm center. The gray box shows the region where data are averaged in the y-direction for subsequent figures. The “C” letter denotes the center of a mesovortex cyclonic circulation.

13. Vertical cross sections of radar reflectivity averaged between ~ 0 – 6 km in the +y-direction (see Fig. 12) from (a) HIWRAP Ku band data valid at ~ 2040 UTC 16 September (b) NOAA P3 X band data valid at ~ 2042 UTC 16 September. Note that there is no data on the right side of (a) due to the HIWRAP coverage and cross section cut.

14. As in Fig. 13, only for radial winds. The gray line denotes the western eye-eyewall interface using the gradient in reflectivity.

15. As in Fig. 14, only for vertical winds. The large gray arrows highlight features discussed in the text.

16. HIWRAP vertical cross sections of Ku band reflectivity (shading; dBZ) and tangential winds (contours;  $\text{m s}^{-1}$ ) at nadir for the Global Hawk overpasses on 17 September centered at (a) 0012 UTC in southeast to northwest direction (b) 0345 UTC in southwest to northeast direction (c) 0550 UTC in southeast to northwest direction and (d) 0805 UTC in southeast to northwest direction.

995

996 17. Conceptual diagram highlighting the measurements and analysis from the HIWRAP,  
997 HAMSR and P3 instruments during the Hurricane Karl (2010) sampling. The arrows  
998 represent the mesoscale flow with red indicating anomalously warm, buoyant air.

999

1000 A1. Scatter plot of HIWRAP horizontal wind speed errors ( $|HIWRAP - P3 \text{ flight level}|$ )  
1001 vs. P3 flight level wind speeds for the coordinated flight during HS3 on 25 Sept. 2013.  
1002 The points are colored by HIWRAP Ku band reflectivity. Note the HIWRAP winds are  
1003 computed using Ku band Doppler velocities. See text for more details.

1004

1005 A2. As in Fig. A1, only for the coordinated flight during GRIP (sampling of Hurricane  
1006 Karl on 16 Sept. 2010 at  $\sim 2040$  UTC). The points are colored by HIWRAP Ku band  
1007 reflectivity. Note the HIWRAP winds are computed using a combination of Ku and Ka  
1008 band Doppler velocities. See text for more details.

1009

1010

1011

1012

1013

1014

1015

1016

1017

1018

1019

1020

1021

1022

1023

1024

1025

1026

## Figures

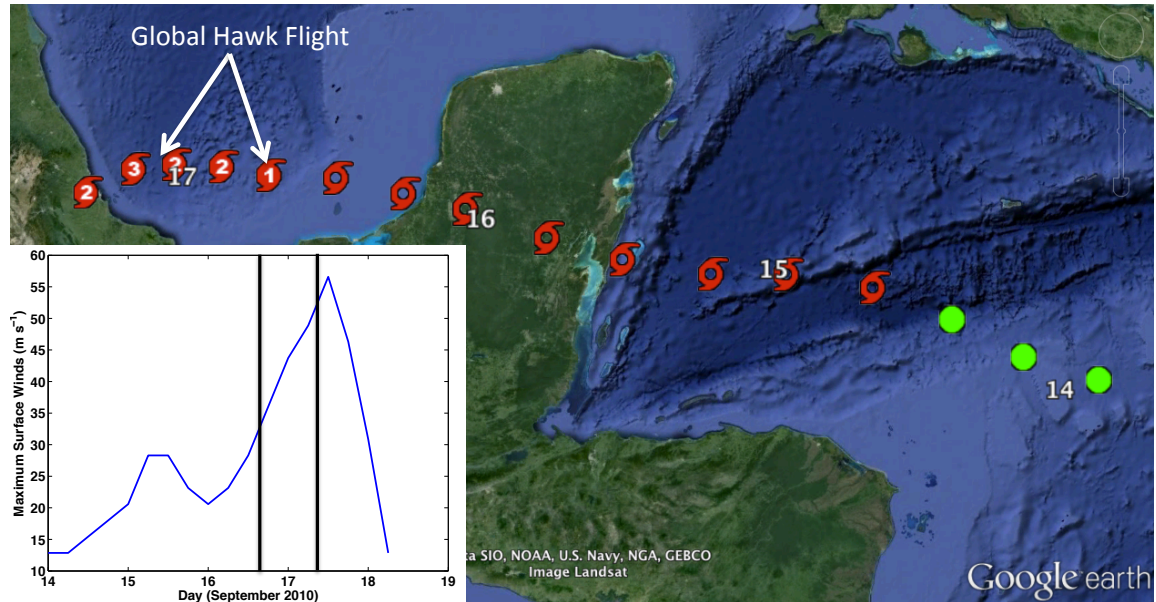


Figure 1. Best track of Hurricane Karl (2010) starting from 0000 UTC 14 September with intensity classifications marked every six hours. The days in September at 0000 UTC are also shown. The green circles denote tropical depression status, open hurricane symbols are tropical storm and closed hurricane symbols are hurricane status with the category listed in the center. The inset shows the time series of maximum surface wind speed in  $\text{m s}^{-1}$  with the Global Hawk flight bracketed with the black lines.

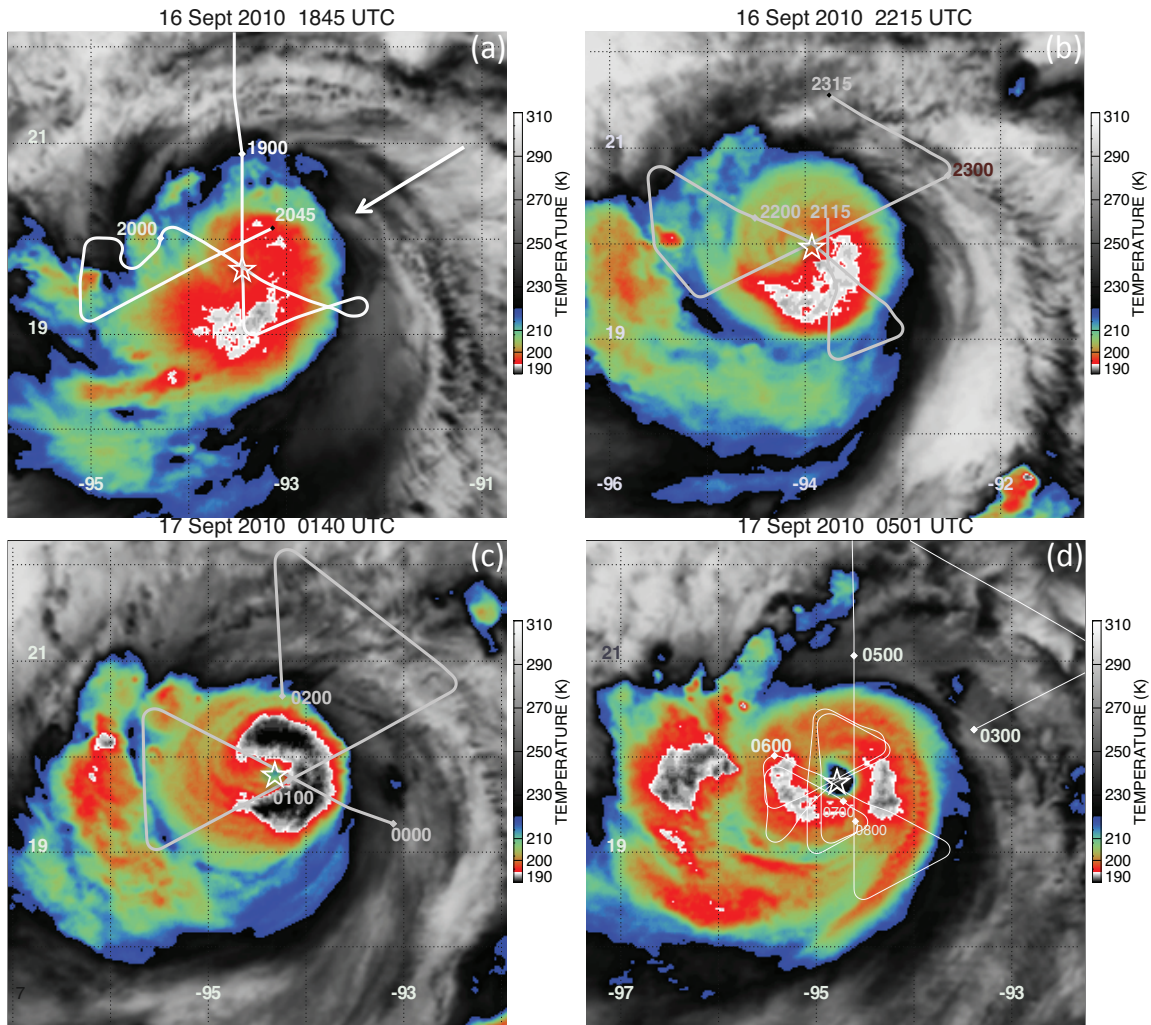


Figure 2. A sequence of GOES IR images of Hurricane Karl (2010) in the Bay of Campeche during an RI episode spanning the GH flights into the storm. The times shown are (a) 1845 UTC 16 September, (b) 2215 UTC 16 September, (c) 0140 UTC 17 September and (d) 0501 UTC 17 September. The white arrow in (a) denotes the environmental vertical wind shear vector valid over the time interval. The star represents the estimated storm center. The track of the GH  $\pm$  2 h from the satellite time stamp is shown in white with the large numbers denoting the hour (UTC).

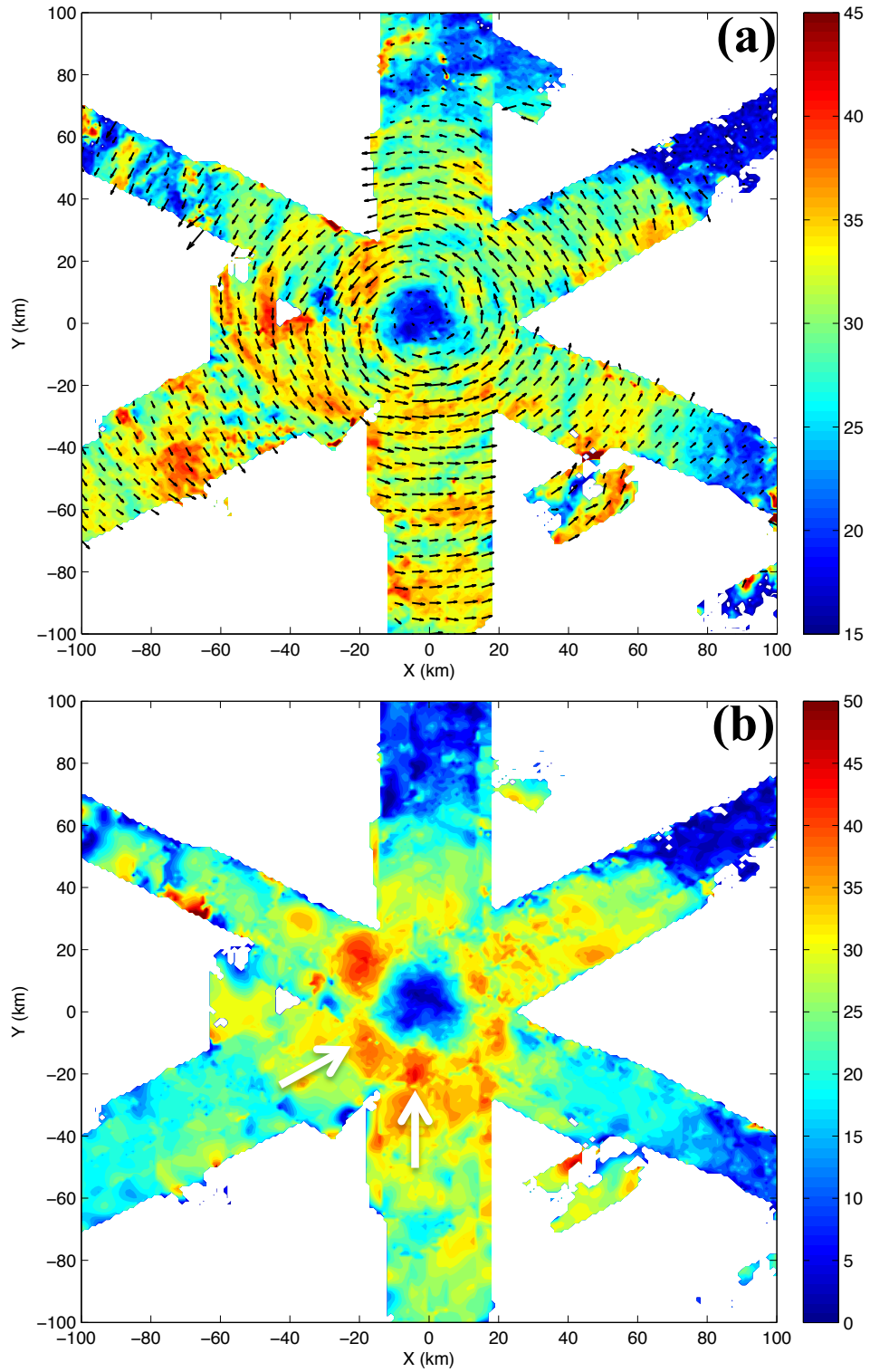


Figure 3. Composite analysis of HIWRAP data averaged over the total Global Hawk sampling interval (12 – 13 h) at 2 km height for (a) Ku band reflectivity (dBZ) and horizontal wind vectors and (b) horizontal wind speeds ( $\text{m s}^{-1}$ ). The white arrows in (b) highlight anomalously large wind speeds in the eyewall discussed in the text.



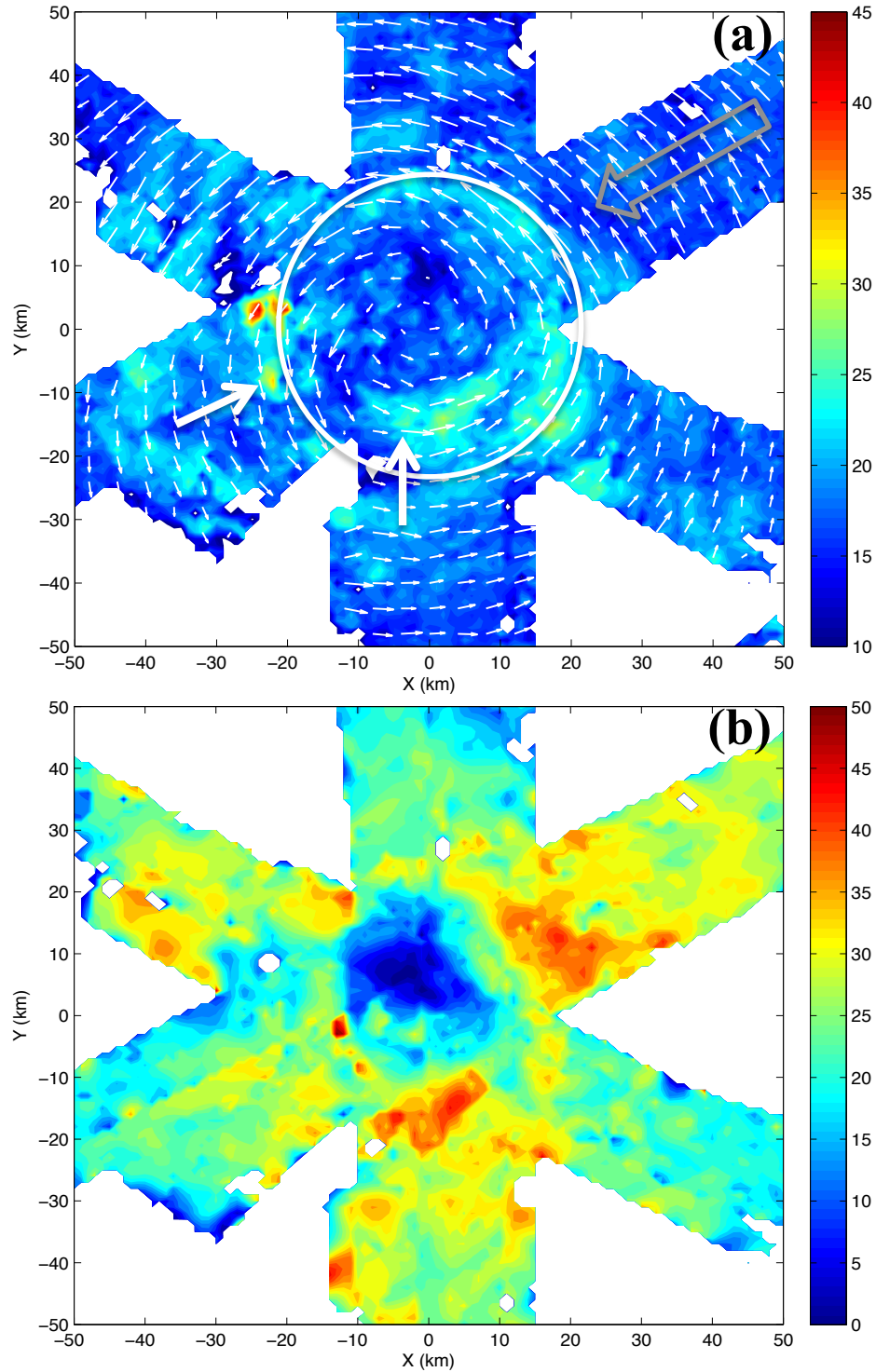


Figure 4. As in Fig. 3 only at 8 km height and zoomed in on the inner-core of Karl. The large, gray arrow in (a) is the large-scale vertical wind shear vector valid for this time interval with a value of  $\sim 5 \text{ m s}^{-1}$ . The thick white arrows in (a) show the locations of low-level (2 km) anomalously large wind speeds in the eyewall (see Fig. 3b). The white circle in (a) shows the location of the low-level (2 km), time and azimuthally averaged RMW.

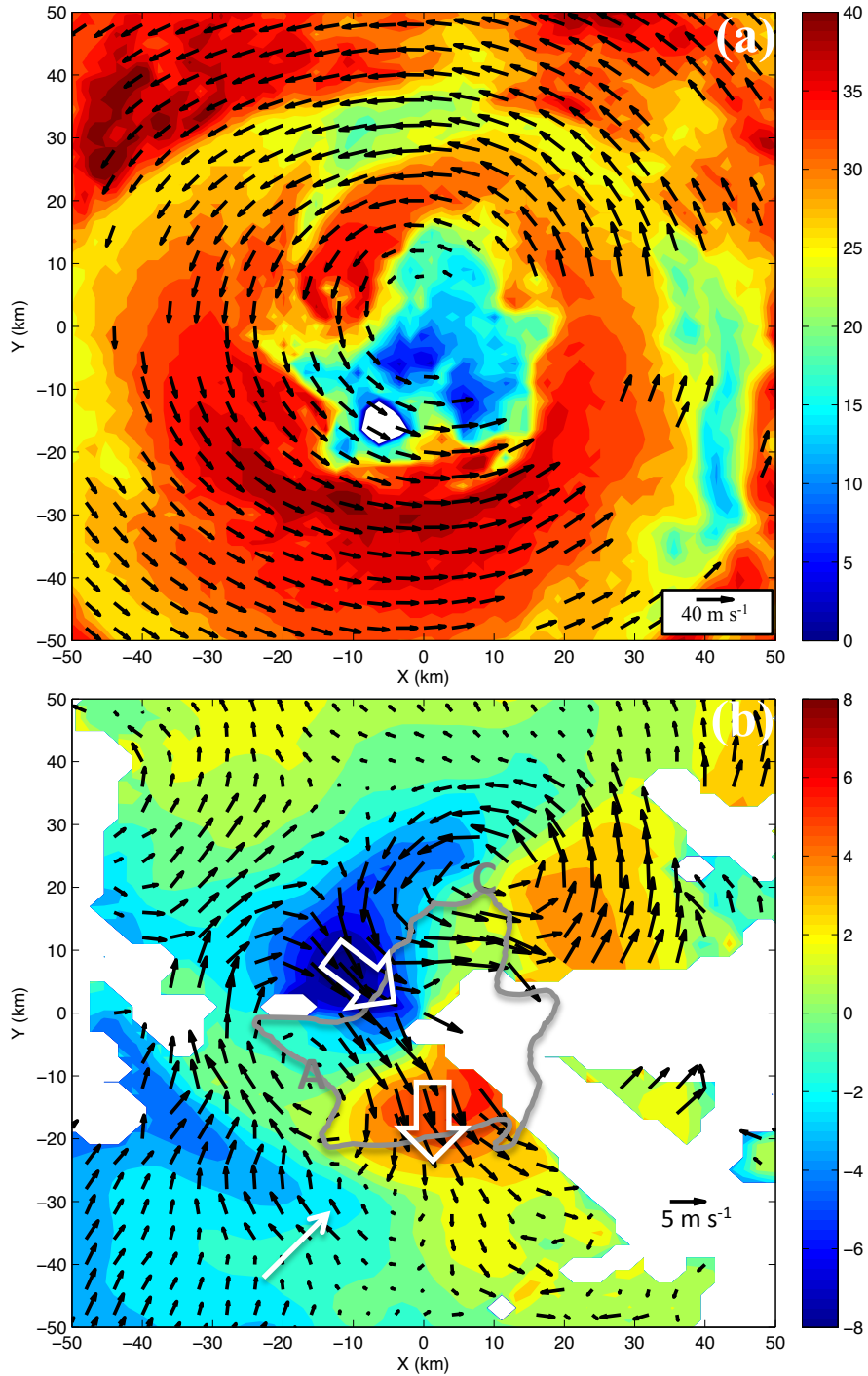
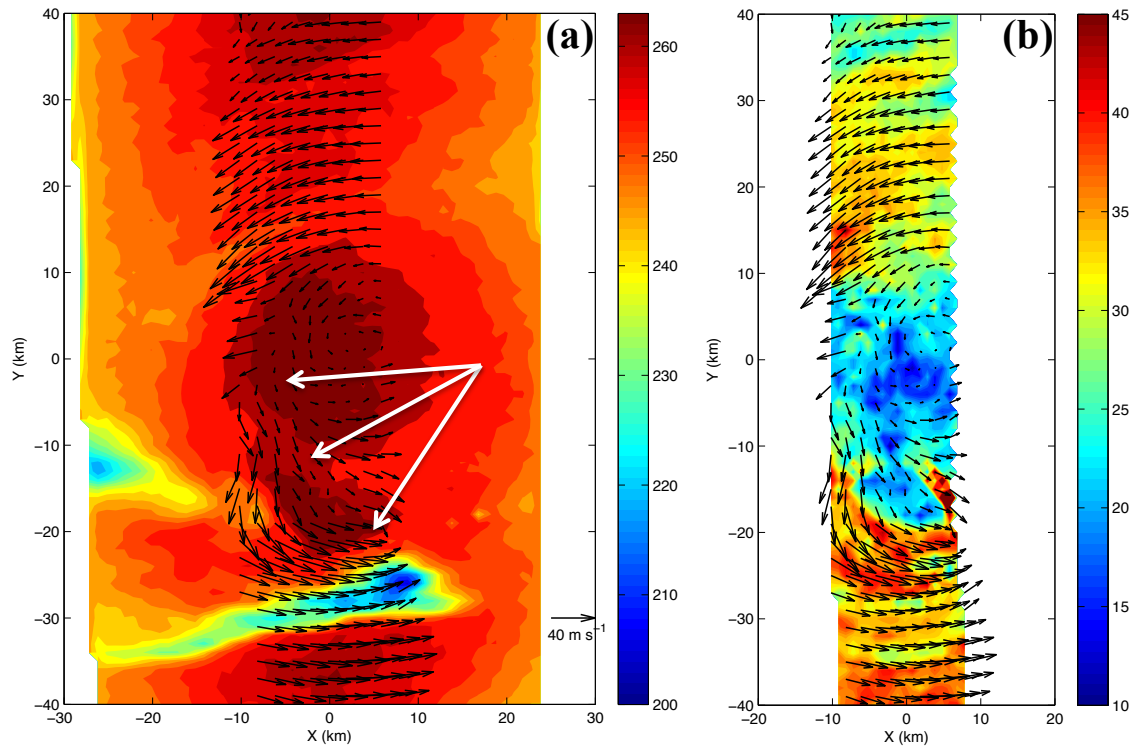


Figure 5. NOAA P3 flight through the inner-core of Hurricane Karl (2010) centered at ~1842 UTC 16 September showing (a) LF C-band reflectivity at 3.7 km height overlaid with TA derived winds at 4 km height and (b) TA derived radial wind speeds averaged between 1 – 4 km height overlaid with perturbation wind vectors averaged over the same interval. The white arrows in (b) highlight features discussed in the text. The gray line in (b) marks the eye-eyewall interface using the gradient in LF reflectivity. The “C” and “A” letters in (b) denote the centers of cyclonic and anti-cyclonic mesovortex circulations, respectively.



1080  
1081



1082  
1083  
1084  
1085  
1086  
1087  
1088  
1089  
1090  
1091  
1092  
1093  
1094  
1095  
1096  
1097  
1098  
1099  
1100  
1101  
1102  
1103  
1104  
1105

Figure 6. Global Hawk overpass of the inner-core of Hurricane Karl (2010) between 1853 – 1919 UTC 16 September showing (a) HAMS 54 GHz Tbs (K) and (b) HIWRAP Ku band reflectivity (dBZ). In both figures, horizontal wind vectors from HIWRAP are overlaid and the analysis level is 2 km height. The white arrows in (a) highlight a protrusion of the warm core discussed in the text. The reference wind vector in (a) applies to both figures. Note that the azimuthal mean RMW at this time and level is  $\sim 30$  km.

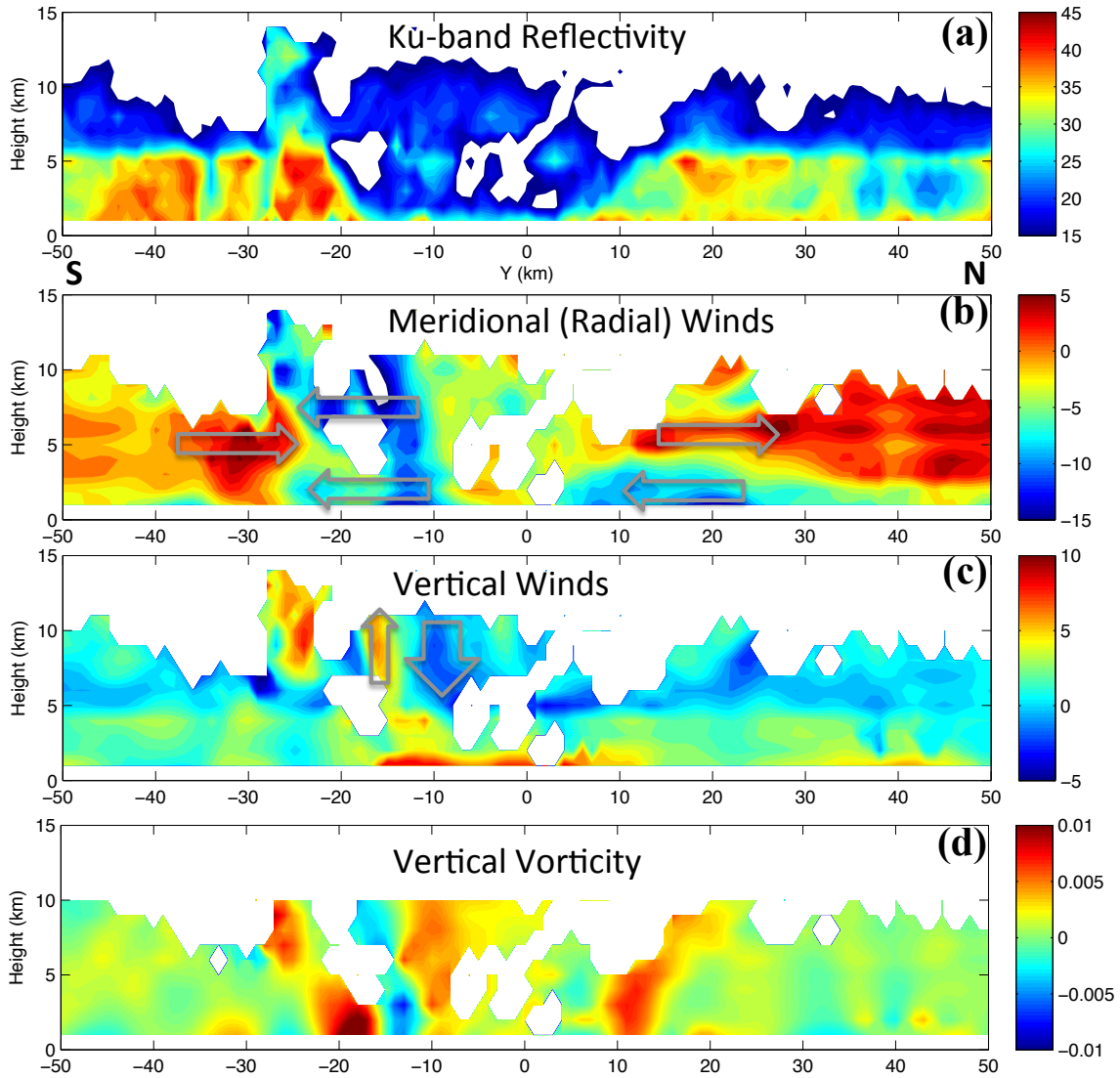


Figure 7. HIWRAP vertical cross sections at nadir through the storm center in the North-South direction for the Global Hawk overpass between 1853 – 1919 UTC 16 September. The data shown is (a) Ku band reflectivity (dBZ), (b) meridional (radial) winds ( $\text{m s}^{-1}$ ), (c) vertical winds ( $\text{m s}^{-1}$ ) and (d) vertical vorticity ( $\text{s}^{-1}$ ). The large gray arrows in (b) and (c) highlight features discussed in the text.

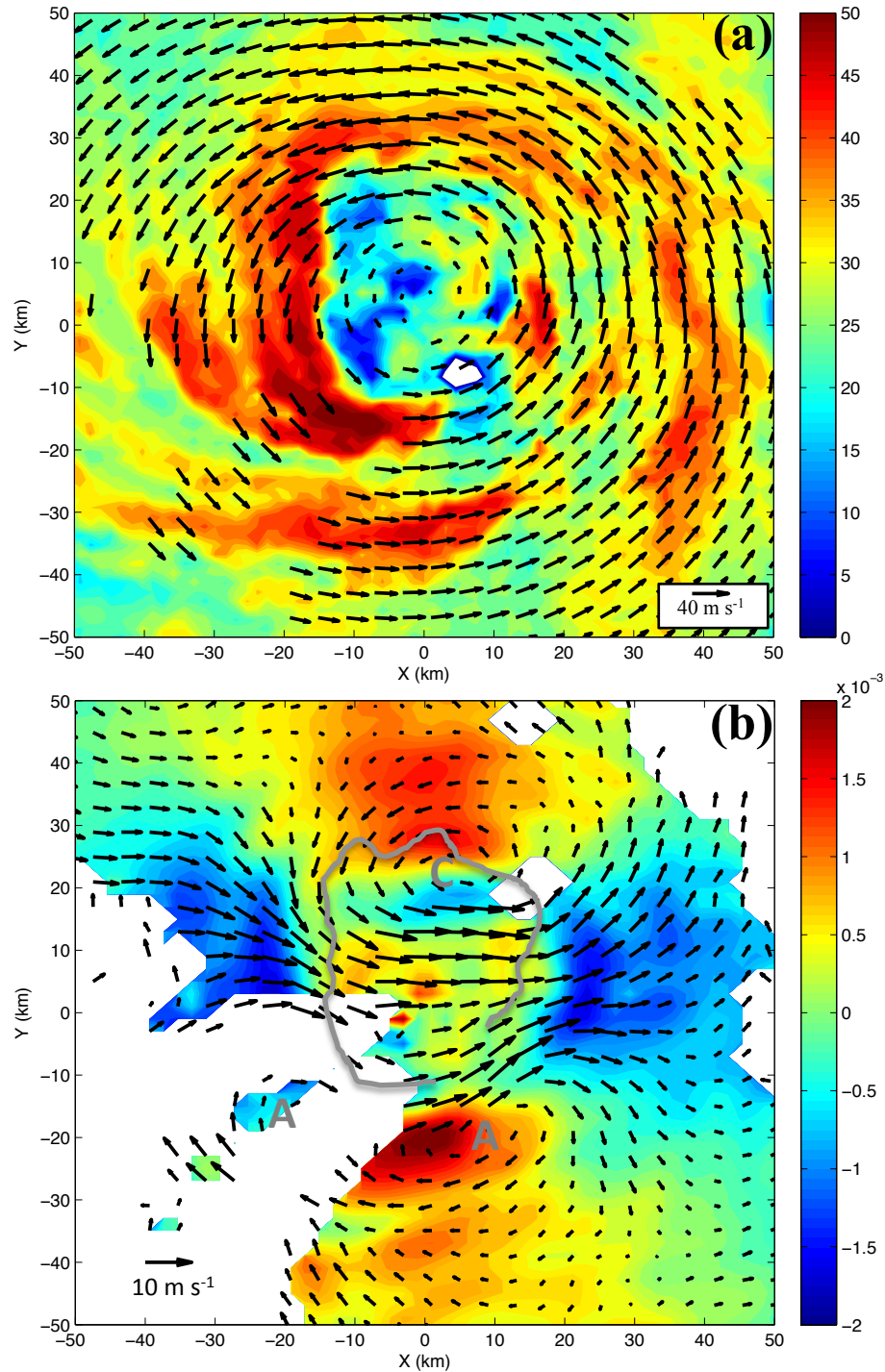
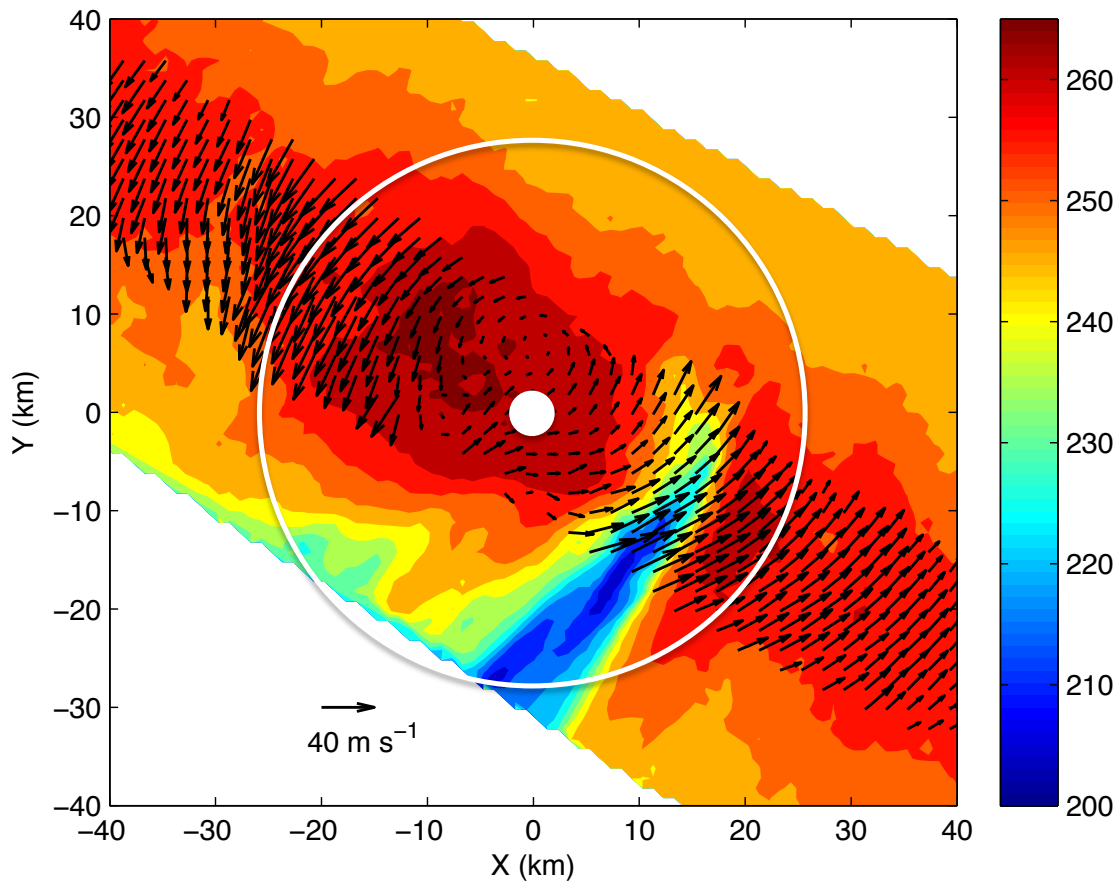


Figure 8. NOAA P3 flight through the inner-core of Hurricane Karl (2010) centered at ~1930 UTC 16 September showing (a) LF reflectivity at 3.6 km height overlaid with TA derived winds at 4 km height and (b) TA derived divergence (s<sup>-1</sup>) averaged between 1 – 4 km height overlaid with perturbation winds averaged over the same interval. The gray line in (b) marks the eye-eyewall interface using the gradient in LF reflectivity. The “C” and “A” letters in (b) denote the centers of cyclonic and anti-cyclonic mesovortex circulations, respectively.

1130  
1131  
1132  
1133  
1134  
1135  
1136  
1137



1138  
1139  
1140  
1141  
1142  
1143  
1144  
1145  
1146  
1147  
1148  
1149  
1150  
1151  
1152

Figure 9. As in Fig. 6a, but for the GH overpass between 1938 – 1957 UTC 16 September. The large white circle denotes the azimuthally averaged RMW at 2 km height and the white dot is the storm center.

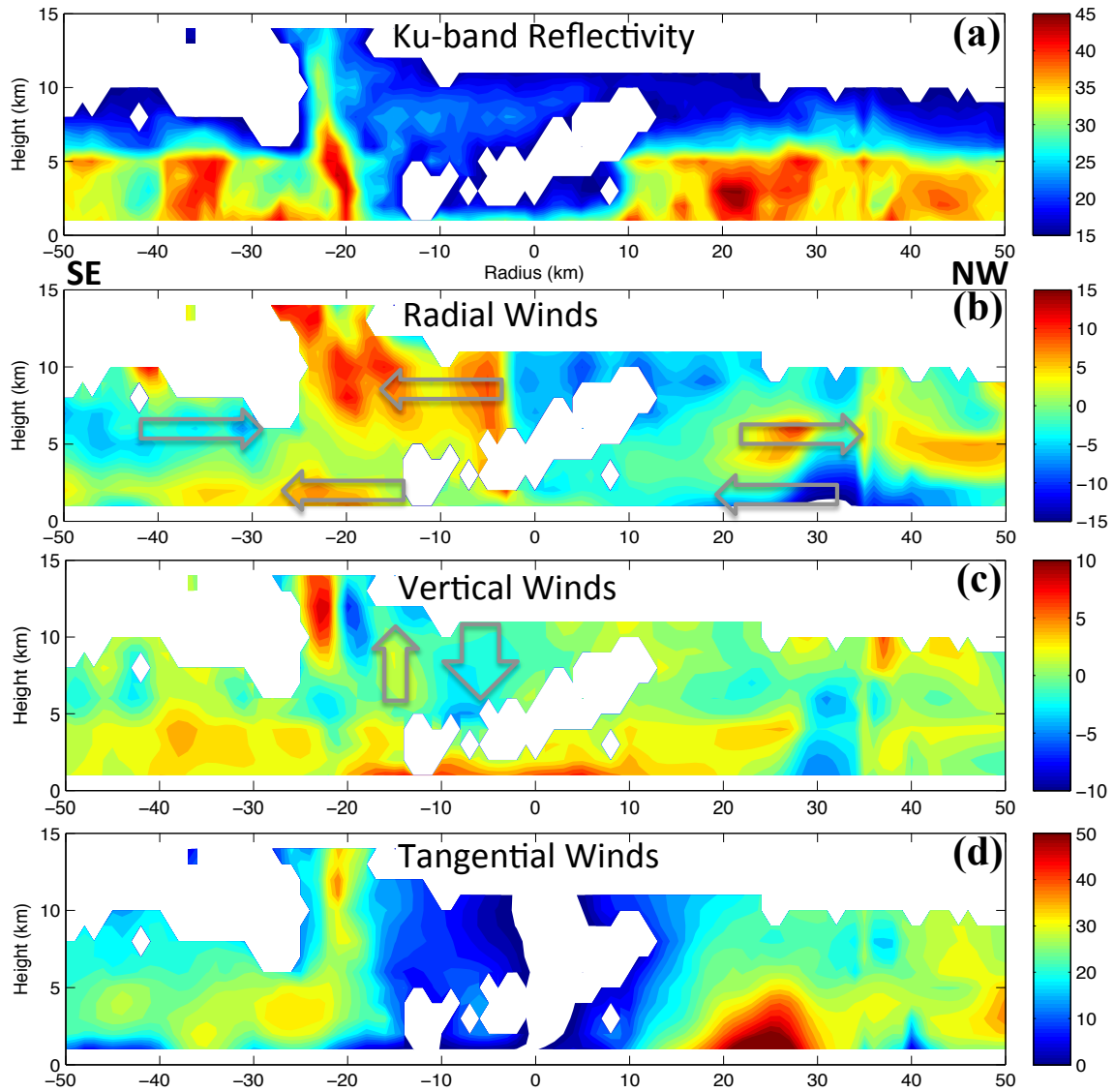


Figure 10. As in Fig. 7 except for the Global Hawk overpass between 1938 – 1957 UTC 16 September in the southeast (negative radius) to northwest (positive radius) direction. The data shown is (a) Ku band reflectivity (dBZ), (b) radial winds ( $\text{m s}^{-1}$ ), (c) vertical winds ( $\text{m s}^{-1}$ ) and (d) tangential winds ( $\text{m s}^{-1}$ ). The gray arrows in (b) and (c) highlight features discussed in the text.

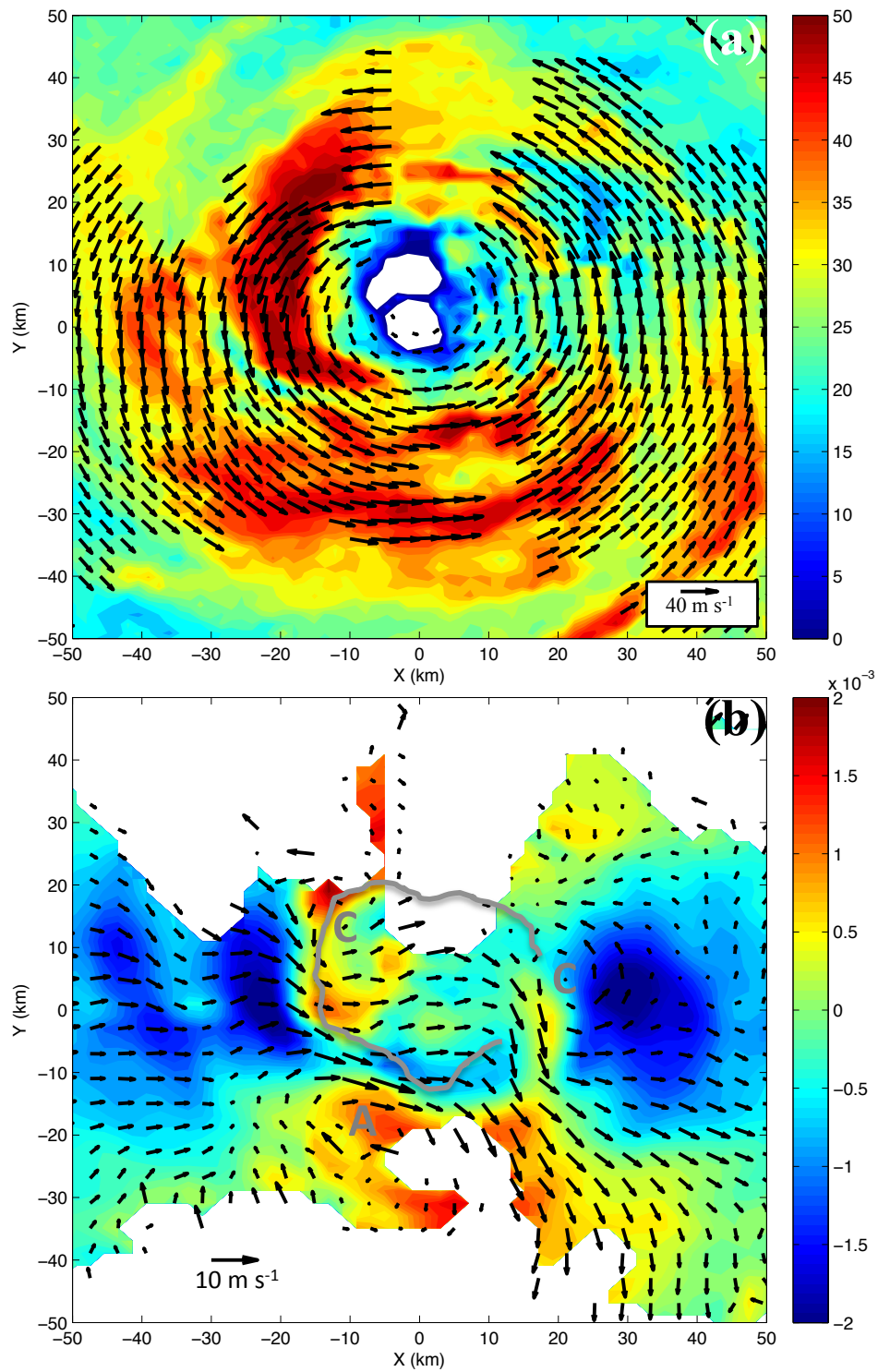


Figure 11. As in Fig. 8, only for the NOAA P3 transect centered at  $\sim 2042$  UTC 16 September.

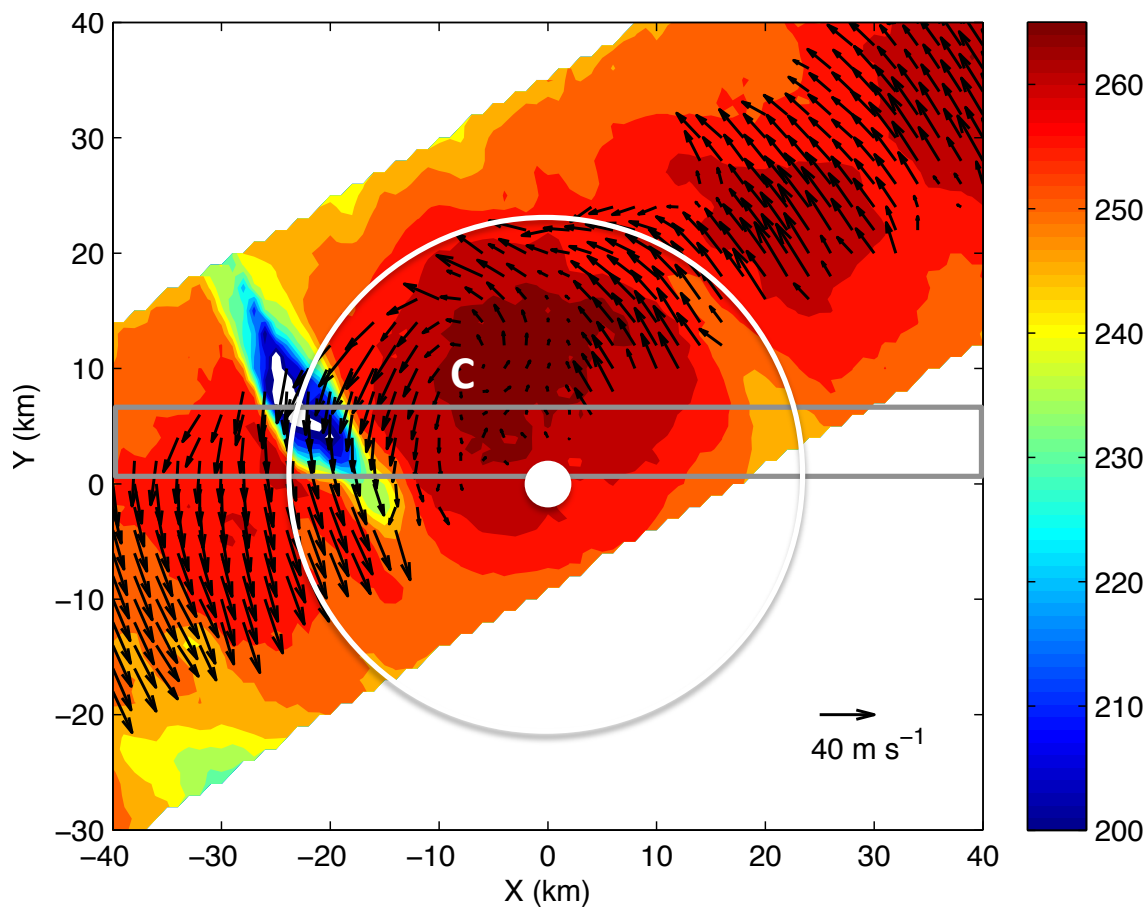
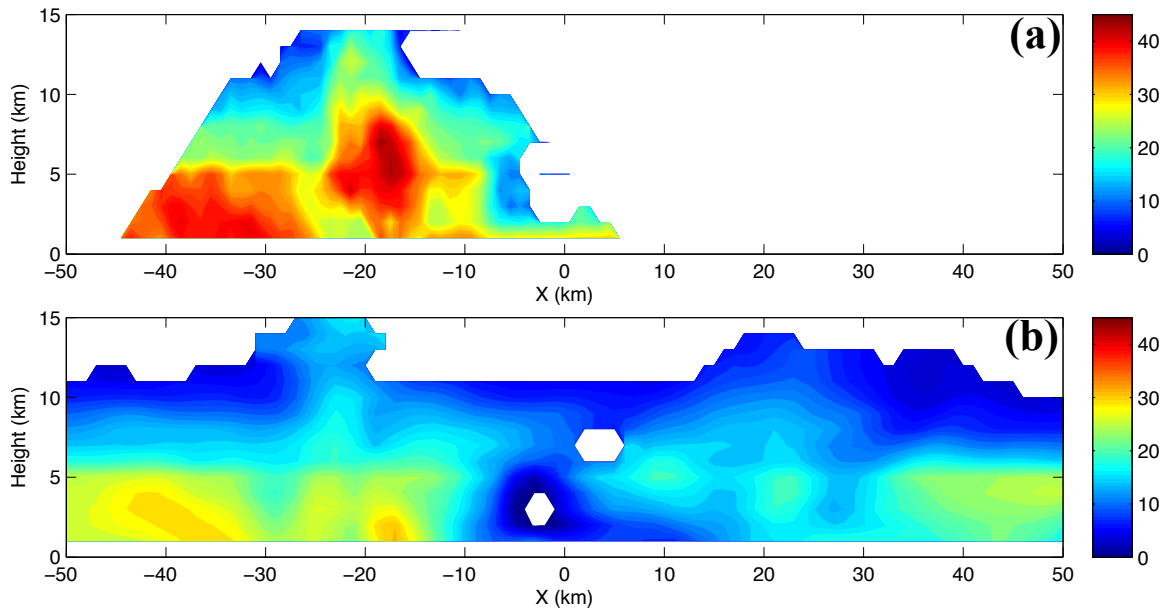


Figure 12. As in Fig. 6a, but for the GH overpass between 2009 – 2055 UTC 16 September with a center crossing at  $\sim 2040$  UTC. The large white circle denotes the azimuthally averaged RMW at 2 km height and the white dot is the storm center. The gray box shows the region where data are averaged in the y-direction for subsequent figures. The “C” letter denotes the center of a mesovortex cyclonic circulation.



1187

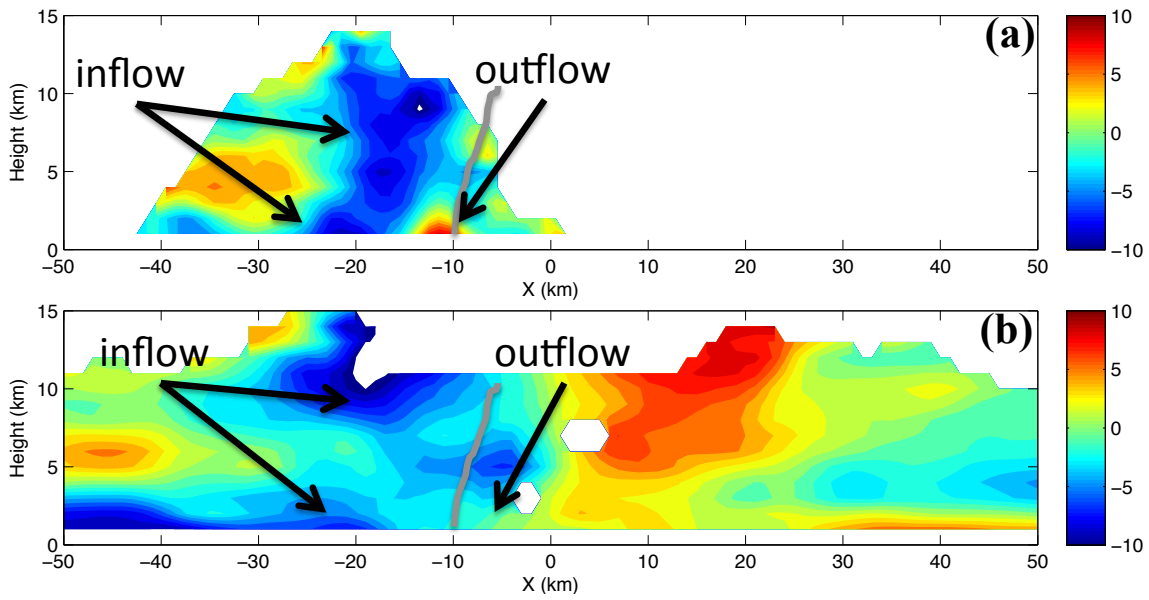


1188  
1189 Figure 13. Vertical cross sections of radar reflectivity averaged between  $\sim 0 - 6$  km in  
1190 the +y-direction (see Fig. 12) from (a) HIWRAP Ku band data valid at  $\sim 2040$  UTC 16  
1191 September (b) NOAA P3 X band data valid at  $\sim 2042$  UTC 16 September. Note that  
1192 there is no data on the right side of (a) due to the HIWRAP coverage and cross section  
1193 cut.  
1194

1195  
1196  
1197  
1198  
1199  
1200  
1201  
1202  
1203  
1204  
1205  
1206  
1207  
1208  
1209  
1210  
1211  
1212  
1213  
1214  
1215  
1216



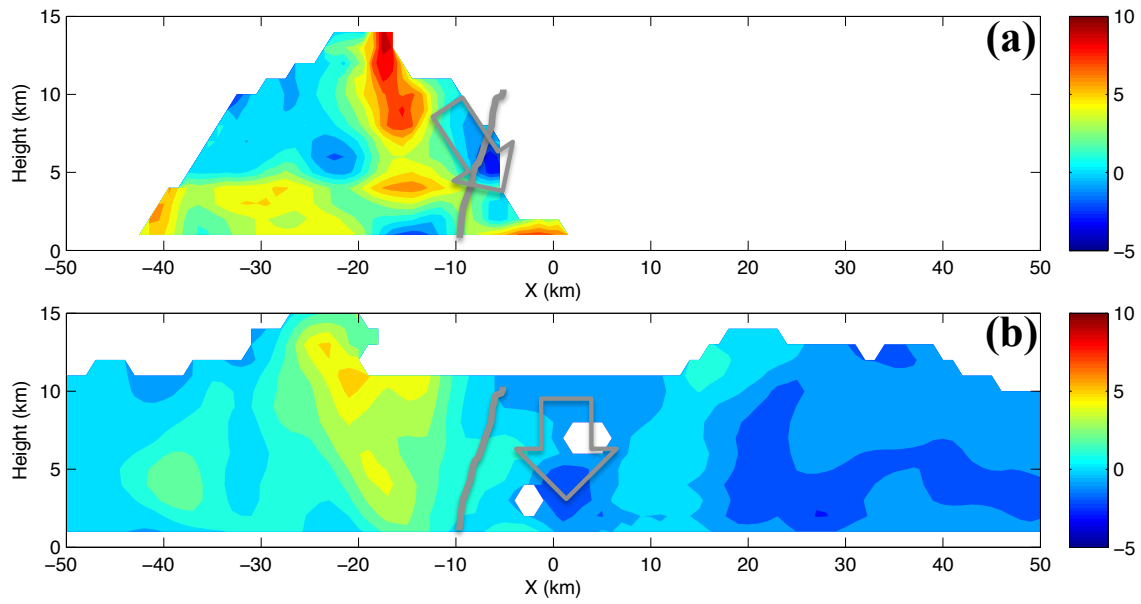
1217  
1218  
1219



1220  
1221  
1222  
1223  
1224  
1225  
1226  
1227  
1228  
1229  
1230  
1231  
1232  
1233  
1234  
1235  
1236  
1237  
1238  
1239  
1240  
1241  
1242  
1243  
1244  
1245  
1246  
1247

Figure 14. As in Fig. 13, only for radial winds. The gray line denotes the western eye-eyewall interface using the gradient in reflectivity.

1248  
1249  
1250  
1251



1252  
1253  
1254  
1255  
1256  
1257  
1258  
1259  
1260  
1261  
1262  
1263  
1264  
1265  
1266  
1267  
1268  
1269  
1270  
1271  
1272  
1273  
1274  
1275  
1276  
1277

Figure 15. As in Fig. 13, only for vertical winds. The gray line denotes the western eye-eyewall interface using the gradient in reflectivity. The large gray arrows highlight features discussed in the text.

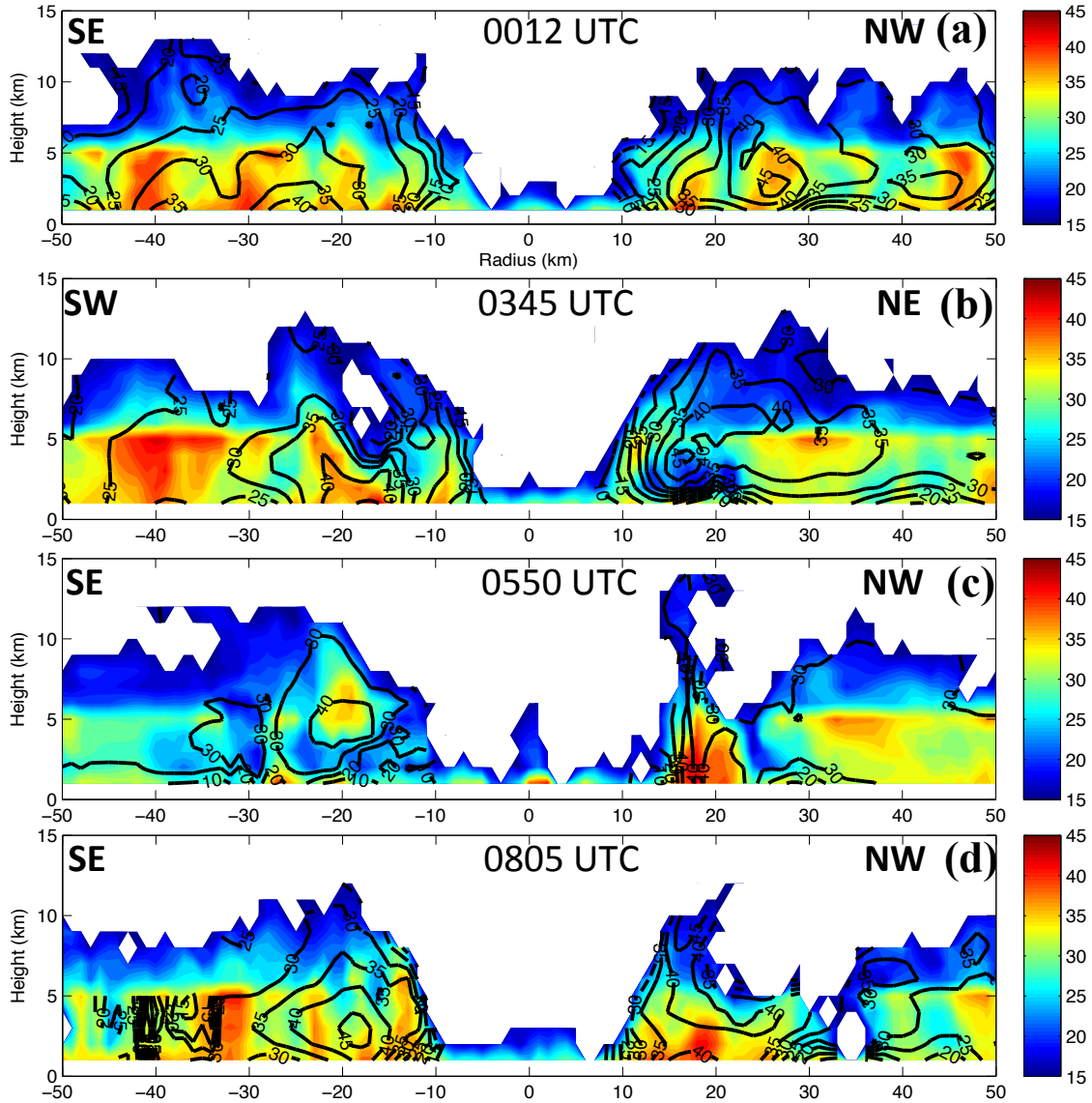


Figure 16. HIWRAP vertical cross sections of Ku band reflectivity (shading; dBZ) and tangential winds (contours;  $\text{m s}^{-1}$ ) at nadir for the Global Hawk overpasses on 17 September centered at (a) 0012 UTC in southeast to northwest direction (b) 0345 UTC in southwest to northeast direction (c) 0550 UTC in southeast to northwest direction and (d) 0805 UTC in southeast to northwest direction.

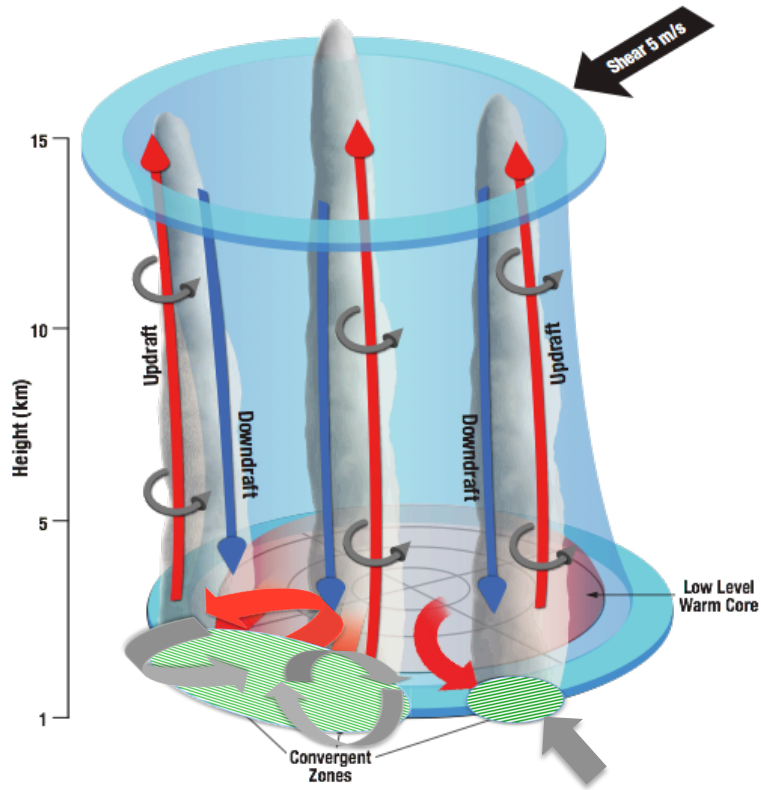


Figure 17. Conceptual diagram highlighting the measurements and analysis from the HIWRAP, HAMSR and P3 instruments during the Hurricane Karl (2010) sampling. The arrows represent the mesoscale flow with red indicating anomalously warm, buoyant air.

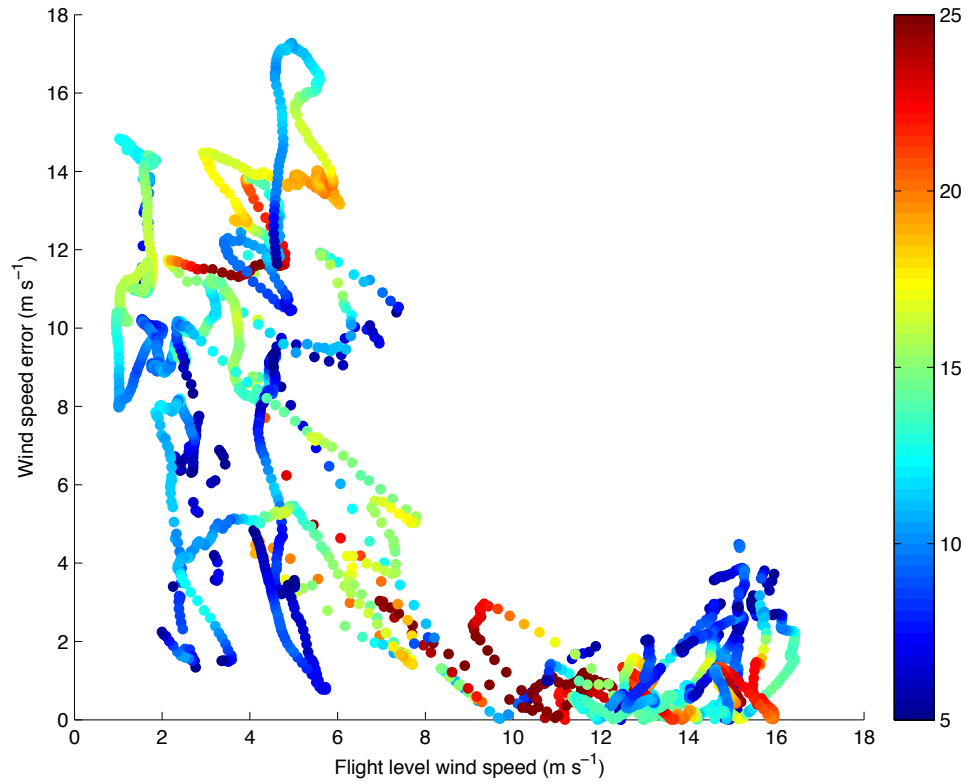
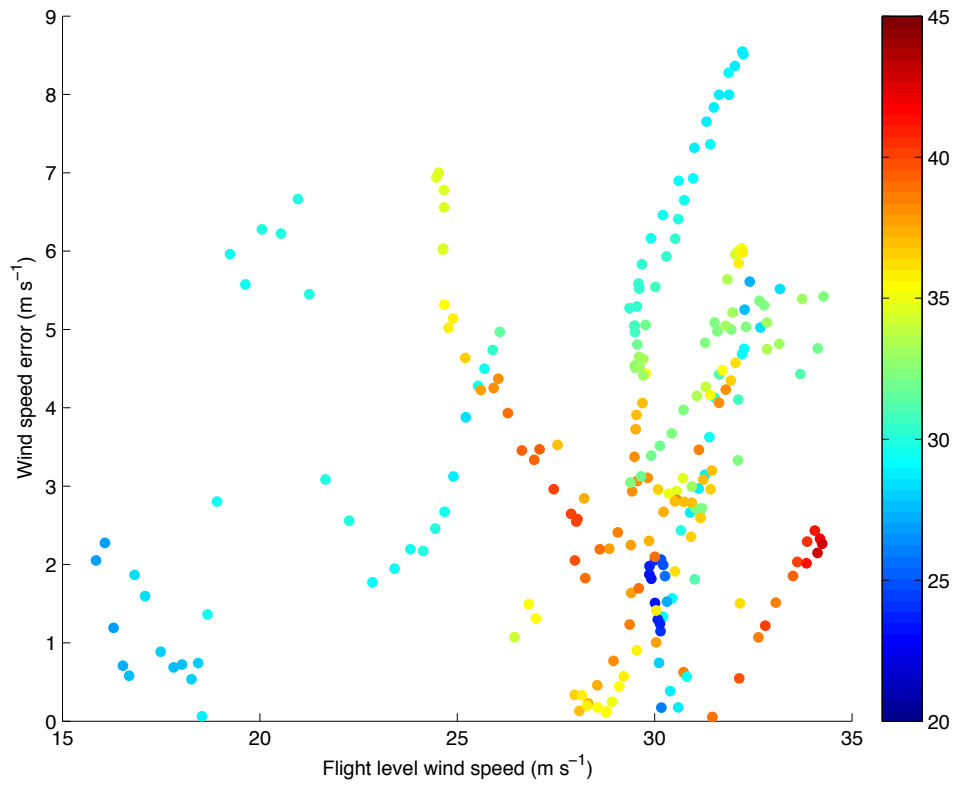


Figure A1. Scatter plot of HIWRAP horizontal wind speed errors ( $|\text{HIWRAP} - \text{P3 flight level}|$ ) vs. P3 flight level wind speeds for the coordinated flight during HS3 on 25 Sept. 2013. The points are colored by HIWRAP Ku band reflectivity. Note the HIWRAP winds are computed using Ku band Doppler velocities. See text for more details.

1332  
1333  
1334



1335  
1336  
1337  
1338  
1339  
1340  
1341

Figure A2. As in Fig. A1, only for the coordinated flight during GRIP (sampling of Hurricane Karl on 16 Sept. 2010 at  $\sim 2040$  UTC). The points are colored by HIWRAP Ku band reflectivity. Note the HIWRAP winds are computed using a combination of Ku and Ka band Doppler velocities. See text for more details.